

Role of cryptic amphibole crystallization in magma differentiation at Hudson volcano, Southern Volcanic Zone, Chile

David J. Kratzmann · Steven Carey ·
Roberto A. Scasso · Jose-Antonio Naranjo

Received: 25 February 2009 / Accepted: 9 July 2009
© Springer-Verlag 2009

Abstract Hudson volcano (Chile) is the southern most stratovolcano of the Andean Southern Volcanic Zone and has produced some of the largest Holocene eruptions in South America. There have been at least 12 recorded Holocene explosive events at Hudson, with the 6700 years BP, 3600 years BP, and 1991 eruptions the largest of these. Hudson volcano has consistently discharged magmas of similar trachyandesitic and trachydacitic composition, with comparable anhydrous phenocryst assemblages, and pre-eruptive temperatures and oxygen fugacities. Pre-eruptive storage conditions for the three largest Holocene events have been estimated using mineral geothermometry, melt inclusion volatile contents, and comparisons to analogous high pressure experiments. Throughout the Holocene, storage of the trachyandesitic magmas occurred at depths between 0.2 and 2.7 km at approximately $\sim 972^{\circ}\text{C}$ (± 25) and $\log f\text{O}_2$ -10.33 – -10.24 (± 0.2) (one log unit above the NNO buffer), with between 1 and 3 wt% H_2O in the melt. Pre-eruptive storage of the trachydacitic magma occurred

between 1.1 and 2.0 km, at $\sim 942^{\circ}\text{C}$ (± 26) and $\log f\text{O}_2$ -10.68 (± 0.2), with ~ 2.5 wt% H_2O in the melt. The evolved trachyandesitic and trachydacitic magmas can be derived from a basaltic parent primarily via fractional crystallization. Entrapment pressures estimated from plagioclase-hosted melt inclusions suggest relatively shallow levels of crystallization. However, trace element data (e.g., Dy/Yb ratio trends) suggests amphibole played an important role in the differentiation of the Hudson magmas, and this fractionation is likely to have occurred at depths >6 km. The absence of a garnet signal in the Hudson trace element data, the potential staging point for differentiation of parental mafic magmas [i.e., ~ 20 km (e.g., Annen et al. in *J Petrol* 47(3):505–539, 2006)], and the inferred amphibolite facies [~ 24 km (e.g., Rudnick and Fountain in *Rev Geophys* 33:267–309, 1995)] combine to place some constraint on the lower limit of depth of differentiation (i.e., ~ 20 – 24 km). These constraints suggest that differentiation of mantle-derived magmas occurred at upper-mid to lower crustal levels and involved a hydrous mineral assemblage that included amphibole, and generated a basaltic to basaltic andesitic composition similar to the magma discharged during the first phase of the 1991 eruption. Continued fractionation at this depth resulted in the formation of the trachyandesitic and trachydacitic compositions. These more evolved magmas ascended and stalled in the shallow crust, as suggested by the pressures of entrapment obtained from the melt inclusions. The decrease in pressure that accompanied ascent, combined with the potential heating of the magma body through decompression-induced crystallization would cause the magma to cross out of the amphibole stability field. Further shallow crystallization involved an anhydrous mineral assemblage and may explain the lack of phenocrystic amphibole in the Hudson suite.

Communicated by T.L. Grove.

Electronic supplementary material The online version of this article (doi:10.1007/s00410-009-0426-1) contains supplementary material, which is available to authorized users.

D. J. Kratzmann (✉) · S. Carey
Graduate School of Oceanography, URI, S. Ferry Rd.,
Narragansett, RI 02882, USA
e-mail: davidk@gso.uri.edu

R. A. Scasso
Dpto. de Cs. Geológicas,
FCEN, Univ. de Buenos Aires Ciudad Univ., Pab 2, 1 Piso,
1428 Buenos Aires, Argentina

J.-A. Naranjo
Serv. Nacional Geol. y Minería, Casilla, Santiago 10465, Chile

Keywords Hudson volcano · Southern Volcanic Zone · Amphibole crystallization · Magma differentiation · Andean margin

Introduction

Magma generation at subduction zones is largely the result of partial melting of the mantle wedge above the descending slab. The lowering of the peridotite solidus in this area is a consequence of the addition of fluids, released from the slab during dehydration reactions (e.g., Tatsumi 1986; Bebout 1991; Thompson 1992; Hawkesworth et al. 1993; Tatsumi and Eggins 1995). Primary magmas ascend through the mantle wedge and may stall and pond at structural and/or density ‘traps’ such as the crust/mantle boundary. Processes of differentiation (e.g., magma mixing, fractional crystallization, assimilation) are then required to generate the intermediate to silicic compositions typical of subduction zones (Gill 1981; Grove and Kinzler 1986). In an open system environment the felsic residual melts produced from differentiation of mafic sources can ascend into upper crustal levels while density-driven sinking of the mafic cumulates (e.g., Glazner 1994) can complement potential vertical stratification within the continental crust (e.g., Rudnick and Fountain 1995). Therefore, whether the differentiation of these volcanic and magmatic rocks occurs at relatively shallow (~3–10 km, e.g., Gill 1981; Grove and Baker 1984; Sisson and Grove 1993) or deeper (>20 km, e.g., Annen and Sparks 2002; Annen et al. 2006) crustal levels is fundamental to understanding continental crust evolution at convergent margins.

The Southern Volcanic Zone (SVZ) of the South American Andean margin is a segment of subduction that is impacted at its southern boundary by the down-going Chile Rise, resulting in a distinctive gap in volcanism to the south. Hudson volcano is the southernmost center of the SVZ and has been the site of some of the largest Holocene explosive eruptions in southern South America (Naranjo and Stern 1998). The three major Holocene explosive eruptions of Hudson Volcano have consistently produced trachyandesite and trachydacite magmas of similar composition, pre-eruptive temperatures, oxygen fugacities, and phenocryst assemblages. Both deep and shallow differentiation has been inferred along the Andean margin (e.g., Tormey et al. 1991; Feeley and Davidson 1994), and both conditions have been modeled for Hudson volcano, Chile (e.g., López-Escobar et al. 1993; Bitschene and Fernández 1995; Gutiérrez et al. 2005).

An investigation of the nature of the magmatic system that fed the major Holocene explosive eruptions of Hudson volcano has been conducted using intensive parameters

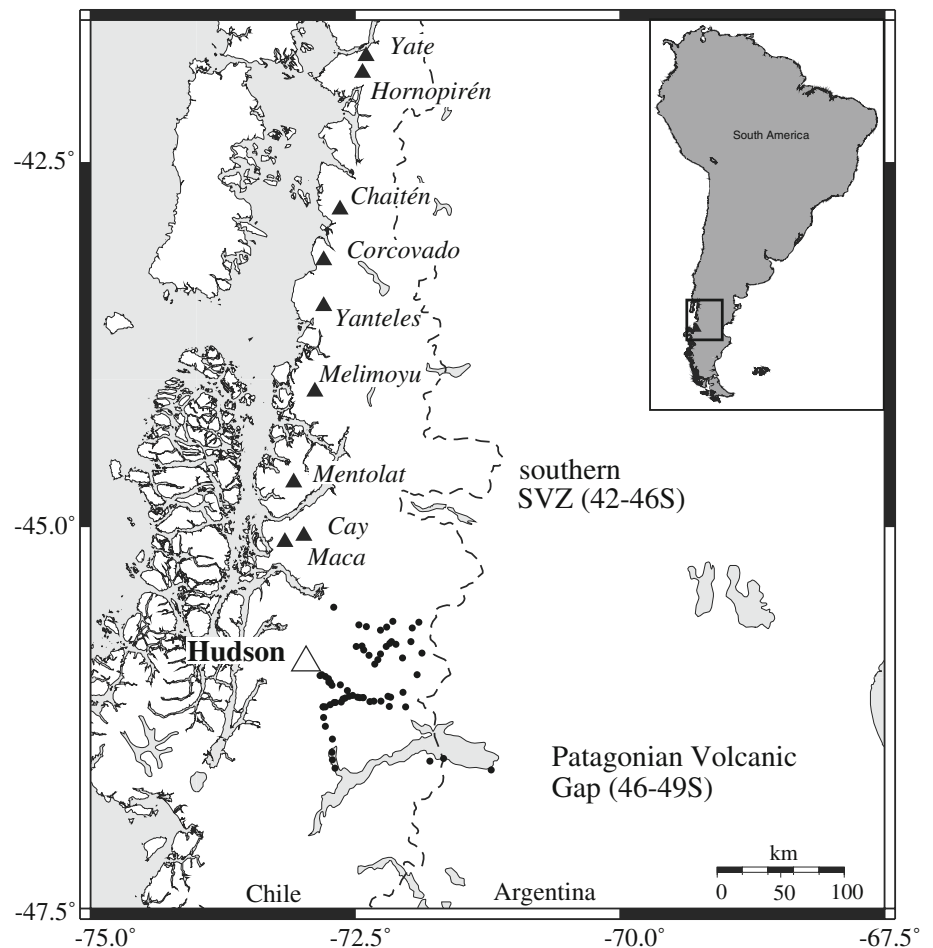
such as pressure, temperature, and volatile content derived from mineral geothermometry, FTIR analyses of melt inclusions, and comparisons with high pressure experiments. The petrogenetic origin of the trachyandesitic and trachydacitic magmas are examined through geochemical modeling of fractional crystallization and magma mixing using a suite of new major and trace element data from the 1991, 3600 years before present (years BP) and 6700 years BP eruptions. In particular, various geochemical proxies [e.g., rare-Earth elements (REE)] have been used to assess the level at which differentiation of parental magmas, to yield more evolved compositions, may have occurred beneath Hudson volcano.

Geological setting and background

Located approximately 280 km from the Nazca–Antarctica–South American triple junction (Naranjo and Stern 1998), Hudson volcano is the southern-most volcano of the Andean SVZ, and is a result of the subduction of the Nazca plate beneath the South American plate (Fig. 1). Subduction of the Chile Rise during the last 8 million years has resulted in the formation of the ~300-km-long Patagonian Volcanic Gap (Stern et al. 1984; Forsythe and Nelson 1985; Stern 2004), with subduction-related volcanism to the south resuming again in the Austral Volcanic Zone (Stern 2004). Hudson volcano has developed on ~30-km-thick crust, surrounded by exposures of tonalitic, granitic, granodioritic, and gabbroic rocks of the Cretaceous to Neogene Patagonian Batholith (Kilian and Behrmann 2003; Gutiérrez et al. 2005). Compositional zonation from leucomonzonite (east) to diorite–tonalite and granodiorite (west) occurs within the batholith (Gutiérrez et al. 2005).

Hudson magmas are medium- to high-K calc-alkaline with elevated incompatible elements [i.e., large-ion lithophile (LILE), high-field strength (HFSE), and REE] relative to other calc-alkaline centers of the SVZ. $^{87}\text{Sr}/^{86}\text{Sr}$ ratios are relatively uniform at ~0.7044, although slightly higher than other volcanoes of the southern SVZ (Naranjo and Stern 1998). Most Hudson compositions plot within the subalkaline field on a total alkali versus silica plot [not shown (e.g., Le Bas et al. 1986, 1992)], and within the calc-alkaline field when plotted on a AFM ternary [not shown (e.g., Irvine and Baragar 1971)]. As such, we have opted to follow the naming convention of previous authors (e.g., Bitschene and Fernández 1995; Naranjo and Stern 1998; Gutiérrez et al. 2005) and designate the Hudson trachyandesites as calc-alkaline. Hudson basaltic magmas have been interpreted as the products of melting and partial assimilation processes occurring during ascent (Gutiérrez et al. 2005). Magma mixing and fractional crystallization can explain the compositional range of the more evolved

Fig. 1 Location map of Hudson volcano (*open triangle*) and the Southern Volcanic Zone (SVZ), South America. Hudson is the southern most center in the SVZ. *Black filled triangles* represent single currently active volcanic centers in the southern SVZ. *Black filled circles* represent sampling locations



magmas erupted at Hudson, such as during the 1991 eruption (Gutiérrez et al. 2005; Kratzmann et al. 2009).

Holocene explosive eruptions

The distribution of tephra layers in southern Patagonia has been used to infer the history of explosive volcanism at Hudson volcano. Active for over the last 1 million years (Orihashi et al. 2004), there have been at least 12 Holocene to Recent explosive eruptions at Hudson (Naranjo and Stern 1998). The 6700 years BP, 3600 years BP, and 1991 eruptions are the largest of these events.

6700 years BP

Stern (1991) geochemically correlated one of the widespread fall deposits in Patagonia to Hudson volcano and radiocarbon dating constrained the age of this eruption to ~6700 years BP (herein referred to as 6700). The stratigraphy of the 6700 eruption contains three major phases, including a thick, laterally extensive accretionary lapilli layer sandwiched between coarse pumice lapilli fall deposits. The lapilli fall deposits represent Plinian pumice fallout from a high altitude plume

(Carey et al. 2005). The extensive accretionary lapilli layer was produced by a large phreatomagmatic phase and can be traced up to 900 km to the south of Hudson volcano. Its bulk volume is estimated at more than 18 km³ [>4 km³ dense rock equivalent (DRE)], making this one of the largest Holocene eruptions in southern South America (Stern 1991).

3600 years BP

Another widespread tephra layer with geochemical affinities to Hudson volcano has been dated at ~3600 years BP (herein referred to as 3600) (Stern 1991). Four stratigraphic units have been identified (P1–P4). The characteristics of units P1, P2, and P4 are representative of fallout from high altitude plumes with minor fluctuations in eruption intensity, whereas P3 resulted from magma/water interactions and a lower eruption column. The volume of the plinian phases of the 3600 eruption have been estimated at ≤ 4 km³ (DRE) (Carey et al. 2005).

1991 eruption

Beginning on 8 August 1991, the initial phase of the eruption involved both phreatomagmatic explosions and

lava flows from a vent and a NNE-SSW trending fissure in the northwestern corner of the caldera (Naranjo et al. 1993). The eruption column from the phreatomagmatic phase reached 12 km elevation and prevailing winds directed the tephra ($\sim 0.2 \text{ km}^2$, bulk volume) to the north and northeast (Scasso et al. 1994; Naranjo and Stern 1998). On 12 August, the paroxysmal phase began with a plinian-style eruption approximately 4 km to the south-southeast of the first phase. After reaching $\sim 10 \text{ km}$ during this initial phase the column height stabilized at $\sim 16 \text{ km}$ on 13 August (Scasso et al. 1994). Localized winds directed the tephra from the column to the southeast in an elongate cloud, extending $\sim 1500 \text{ km}$ to the south and almost 370 km wide. The 1991 eruption produced approximately 4.3 km^3 bulk volume (2.7 km^3 DRE) of pyroclastic material (Scasso et al. 1994; Naranjo and Stern 1998).

Samples and analytical techniques

Tephra fall deposits from the three major Holocene eruptions were sampled at 71 sites along the Chilean–Argentinean border. Overall deposit thicknesses were measured, maximum pumice and lithic sizes recorded, and samples of both the bulk deposits and stratigraphic sub-units were collected for each eruption. With the exception of the ash fall from phase 1 of the 1991 eruption, subsequent petrographic and geochemical analyses were conducted on single or multiple pumice lapilli selected from these tephra layers. Lapilli were first cleaned in de-ionized (DI) water, sonicated for 10 min to remove any foreign particles, rinsed in DI water again and subsequently dried overnight at 100°C .

Whole-rock analyses of multiple pumices were carried out using X-ray fluorescence analysis (XRF) with a Bruker S4 Pioneer wave length dispersive X-ray fluorescence spectrometer at the Department of Geosciences, University of Rhode Island (URI). Precision for most elements was better than 0.2 wt% and accuracy better than 1 wt% of the measured values. Major element compositions of matrix glass and melt inclusions were determined using both the Cameca MBX (for high silica glasses) and Cameca SX-100 (for low silica glasses and mineral phases) electron microprobes located at the Geological Sciences Department at Brown University using the methods described by Devine et al. (1995). All microprobe analyses were better than 0.6 wt% for most elements. Trace element data for matrix glass and melt inclusions were collected using laser ablation inductively coupled plasma mass spectrometry (LA-ICP-MS) with the New Wave 213 nm Nd-YAG laser attached to a Thermo X-Series II quadrupole ICP-MS at the Graduate School of Oceanography (URI) following the methods of Kelley et al. (2003) and calibrated against

USGS, NIST-RSM, and MPI-DING reference glasses. Ti-normalization was used on calibration curves, which were linear, and reproducibility of replicate analyses is $<6\%$ RSD. Water contents (transmission data) were measured on a Thermo Nicolet Nexus 670 Fourier Transform Infra Red (FTIR) spectrometer attached to a Thermo Nicolet Continuum IR microscope at the Department of Earth and Planetary Sciences, American Museum of Natural History, New York City. Modifications to the methods of Mandeville et al. (2002) include 400 scans for each IR spectrum (1024 previously) and an increase in the range of measurements into the near-IR (7500 cm^{-1} compared to 6500 cm^{-1}). The petrologic plotting and modeling programs Iqpet[®] and Mixing[®] (Carr 2005) were used for data inspection and classifications.

Results

Whole-rock data

Whole-rock analyses were conducted on pumice lapilli from the three major Holocene explosive events at Hudson volcano, with the exception of phase 1 of the 1991 eruption (Fig. 2; Table 1). Bulk tephra analysis was conducted on a phase 1 sample even though it has undergone aeolian (i.e., physical) fractionation prior to deposition. Although relatively aphyric ($\sim 2 \text{ vol.}\%$ crystals), the whole-rock major element data are offset from the glasses such that we have

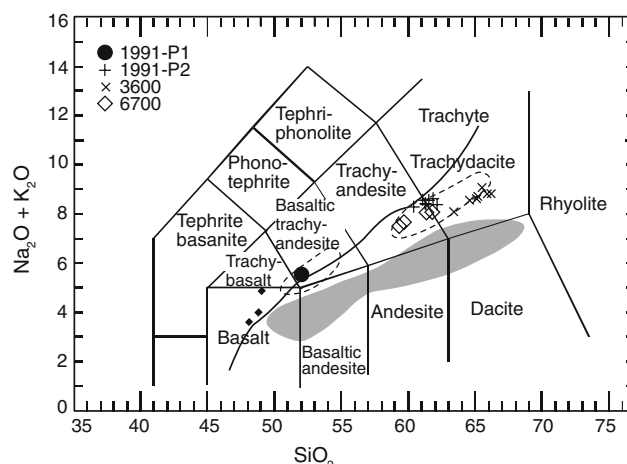


Fig. 2 Whole-rock total alkali versus silica plot (classification from Le Bas et al. 1986). 1991 basalt (black filled circles), 1991 trachyandesite (plus symbol), 3600 (crosses), 6700 (open diamonds). Calc-alkaline products from volcanoes in the Southern Volcanic Zone (gray field) and Hudson volcano (open black dashed fields) from Gutiérrez et al. (2005) and references therein. Río Ibáñez (filled black diamonds) from Gutiérrez et al. (2005). The Hudson samples overlie the curve of Le Bas et al. (1992) dividing the alkaline and subalkaline fields (irregular solid black line)

Table 1 Major and trace element bulk rock compositions of samples from the Holocene eruptions (measured by XRF)

Eruption Phase Unit Sample	1991 P1 ^a HUD110	1991 P1 ^b 210192.1D	1991 P2 D HUD207	1991 P2 D HUD206	1991 P2 C HUD208	1991 P2 C HUD141	1991 P2 B HUD209	1991 P2 B HUD143	1991 P2 A HUD210	1991 P2 A HUD149
SiO ₂	51.61	51.44	59.81	61.01	61.00	61.47	61.56	60.82	61.83	60.92
TiO ₂	2.03	2.15	1.37	1.31	1.32	1.33	1.29	1.30	1.24	1.30
Al ₂ O ₃	15.96	15.79	16.60	16.71	16.76	16.77	16.74	16.49	16.33	16.83
Fe ₂ O ₃	11.55	11.74	6.50	6.20	6.12	6.18	6.05	6.00	5.86	6.04
MnO	0.18	0.19	0.18	0.18	0.18	0.18	0.18	0.18	0.17	0.18
MgO	4.14	4.21	1.92	1.83	1.80	1.75	1.74	1.70	1.69	1.75
CaO	8.27	8.24	4.08	3.94	3.81	3.86	3.73	3.67	3.73	3.67
Na ₂ O	4.31	4.27	5.91	6.10	6.12	6.27	6.18	6.17	5.96	6.17
K ₂ O	1.23	1.22	2.29	2.32	2.35	2.39	2.38	2.39	2.42	2.35
P ₂ O ₅	0.71	0.71	0.48	0.44	0.46	0.46	0.44	0.45	0.42	0.44
LOI	−0.55	—	0.97	0.63	0.09	0.18	0.09	0.11	0.36	0.07
Total	99.99	99.96	100.11	100.67	100.01	100.84	100.38	99.28	100.01	99.72
S	—	—	246	b.d.l	216	b.d.l.	192	b.d.l	232	b.d.l
Sc	—	25	18	b.d.l	15	b.d.l.	16	b.d.l	18	b.d.l
V	343	322	87	73	70	73	59	66	74	71
Cr	32	19	21	0	16	b.d.l.	19	b.d.l	32	b.d.l
Co	30	33	7	11	5	4	6	3	6	8
Ni	12	12	3	5	2	4	2	3	2	3
Cu	51	45	9	8	7	6	6	8	7	5
Zn	120	91	107	101	107	98	104	100	97	99
Ga	21	19	21	20	22	23	21	23	22	22
Rb	34	27	56	57	59	57	59	59	60	59
Sr	546	524	371	374	370	365	369	349	350	354
Y	38	35	47	48	49	49	50	49	47	49
Zr	186	178	362	354	368	360	371	369	381	364
Nb	11	5	21	19	20	19	21	19	20	19
Mo	—	2	—	—	—	—	—	—	—	—
Ba	420	371	711	705	728	704	707	715	721	710
Hf	—	—	10	b.d.l	9	b.d.l	9	b.d.l	10	b.d.l
Pb	18	9	14	13	13	11	12	11	13	10
La	87	18	64	57	56	71	55	64	56	56
Ce	65	49	107	99	96	100	96	104	101	116
Nd	—	30	—	—	—	—	—	—	—	—
Sm	—	9	—	—	—	—	—	—	—	—
Th	15	4	1	7	5	5	5	>1	5	>1
U	22	6	—	>1	—	—	—	—	—	—
Eruption Phase Unit Sample	3600 C HUD134	3600 C HUD202	3600 B HUD203	3600 A HUD204	3600 A HUD136	6700 B HUD212	6700 B HUD186	6700 A HUD174	6700 A HUD187	
SiO ₂	61.07	61.49	62.26	62.65	61.96	57.27	56.56	55.92	57.97	
TiO ₂	1.03	0.91	0.89	0.88	0.88	1.37	1.26	1.38	1.34	
Al ₂ O ₃	16.77	16.94	16.36	16.23	15.56	17.58	15.52	16.53	15.76	
Fe ₂ O ₃	5.08	4.31	4.16	4.33	4.22	6.54	5.15	6.60	5.50	
MnO	0.14	0.13	0.13	0.13	0.13	0.16	0.15	0.17	0.16	
MgO	1.31	0.91	0.94	1.17	0.96	1.91	1.90	2.01	1.96	

Table 1 continued

Eruption Phase Unit Sample	3600 C HUD134	3600 C HUD202	3600 B HUD203	3600 A HUD204	3600 A HUD136	6700 B HUD212	6700 B HUD186	6700 A HUD174	6700 A HUD187
CaO	2.85	2.18	2.21	2.30	2.12	3.89	3.90	3.56	4.12
Na ₂ O	5.10	5.30	5.39	5.36	5.48	5.23	5.75	5.09	5.79
K ₂ O	2.72	2.85	2.92	2.93	3.10	2.09	2.24	2.14	2.29
P ₂ O ₅	0.29	0.22	0.22	0.22	0.22	0.48	0.46	0.42	0.50
LOI	4.80	5.10	4.40	3.80	3.80	3.20	1.70	3.70	1.40
Total	101.16	100.34	99.88	100.00	98.43	99.72	94.59	97.52	96.79
S	–	198	185	170	–	289	–	–	–
Sc	–	13	10	12	–	22	–	–	–
V	77	47	44	43	50	89	93	93	97
Cr	6	18	12	14	>1	22	4	19	0
Co	11	1	2	b.d.l	2	10	7	9	12
Ni	5	3	2	3	4	4	6	14	5
Cu	13	11	8	9	7	14	8	14	11
Zn	82	79	79	83	77	97	98	101	99
Ga	21	21	22	20	20	23	22	23	22
Rb	71	74	74	76	79	51	55	54	54
Sr	253	222	223	217	205	348	351	318	366
Y	51	54	53	54	52	50	52	55	53
Zr	491	547	539	541	528	479	432	490	429
Nb	22	26	26	26	23	25	21	22	21
Mo	–	–	–	–	–	–	–	–	–
Ba	885	879	869	919	950	817	773	773	788
Hf	–	14	13	14	–	15	–	–	–
Pb	11	14	10	15	15	11	14	14	16
La	72	68	60	75	79	75	78	82	88
Ce	120	128	113	143	126	129	126	120	118
Nd	–	–	–	–	–	–	–	–	–
Sm	–	–	–	–	–	–	–	–	–
Th	b.d.l	–	–	–	4	–	6	8	15
U	3	–	–	–	4	–	3	4	9

Published bulk rock data and the average of repeat analysis ($n = 5$) of 1991 basaltic ash fall for comparison

b.d.l. beyond detection limits

^a Data from five repeat analyses of ash fall deposit

^b Data from Bitschene et al. (1993)

used the analyses of the 1991 basaltic glass (i.e., least to most evolved) for geochemical modeling. Whole-rock data on the Hudson basalts are also available in the literature (e.g., Bitschene et al. 1993; López-Escobar et al. 1993; Ippach 2001).

The trachyandesite to trachydacite whole-rock analyses of pumice lapilli from the 6700 and phase 2 of the 1991 eruptions occupy a narrow SiO₂ range, from 59 to 62 wt%. In contrast, whole-rock analyses of pumice lapilli samples from the 3600 eruption are more evolved trachydacitic,

ranging from 63 to 66 wt% SiO₂. Phase 1 of the 1991 eruption is basaltic to basaltic-andesite in composition (50–54 wt% SiO₂).

The major element compositions reported here are similar to those reported by previous authors (e.g., Bitschene and Fernández 1995; Naranjo and Stern 1998; Gutiérrez et al. 2005). The whole-rock compositions of this study and that of Gutiérrez et al. (2005) exhibit a distinctive gap in SiO₂ from ~55 to 60 wt% (Fig. 2). Similar compositional gaps are present in the matrix glass data (this

study). No bulk compositional variations have been identified within individual subunits analyzed from any of the eruptions.

Petrography and mineralogy

Tephra from the 1991 basaltic eruption is relatively crystal poor, black, basaltic vitric ash. The ash collected at Puerto Aisén contains tachylite (~50 vol.%), pale brown, plagioclase-phyric sideromelane (~45 vol.%), lithic clasts (~5 vol.%) and plagioclase, clinopyroxene and Fe–Ti oxide crystals (Bitschene and Fernández 1995). Low vesicularity tachylitic particles are generally blocky with large, ovoid vesicles and a high abundance of intergrown microlites of varying morphologies including tabular, hopper and swallowtail types (Kratzmann et al. 2009). These morphologies are similar to those produced in studies of volatile exsolution-induced crystallization (e.g., Hammer and Rutherford 2002). The tachylitic particles are similar to samples from the 2001 basaltic eruption of Mt Etna (e.g., Taddeucci et al. 2004). Fluidal to irregularly shaped sideromelane fragments are brown in color, more vesicular than the tachylite, and feature a smaller population of larger microlites (Kratzmann et al. 2009).

The 1991 trachyandesite tephra fall deposits are composed of alternating units of pale gray fine ash, and gray pumice lapilli, with sharp contacts between units. The pale gray units are composed of glass shards, pumice, crystal, and lithic fragments (Scasso et al. 1994). Glassy tephra range from pale gray/white tube pumice to dark brown/black, blocky, poorly vesicular shards (Scasso and Carey 2005). The 1991 trachyandesite pumice samples are highly vesicular (Fig. 3a) and vary from dark gray/black to pale brown/tan. Several reworked samples collected from Lago Buenos Aires display prominent color bands that have been previously cited as evidence for magma mingling (e.g., Bitschene and Fernández 1995). Our analysis of the bands reveals similar major element compositions and does not support physical mingling. We attribute these color differences largely to variations in the extent of vesiculation (Kratzmann et al. 2009).

Of the four phases identified for the 3600 eruption, phases one and two are commonly reversely graded, coarse lapilli fall deposits. Phase three deposited a massive, poorly sorted, silty-ash layer with pumice and minor accretionary lapilli. The final phase of the eruption produced a pumice lapilli fall deposit that commonly shows normal grading (Carey et al. 2005). The contacts between units are sharp. Pumice lapilli samples from the 3600 eruption are highly vesicular and vary from pale tan to brown in color.

Three major phases were identified for the 6700 eruption. The initial and final phases produced reversely or normally graded, coarse pumice lapilli fall deposits. The

second phase produced a thick, distinctive accretionary lapilli-rich, silty-ash layer with accretionary lapilli diameters up to 2.3 cm at 35 km from the volcano (Carey et al. 2005). Pumice lapilli samples are typically highly vesicular, vary from pale tan to brown in color, and are very friable (Figs. 3e–h and 4f).

Plagioclase is the dominant phenocryst phase in the products from the three Holocene eruptions being investigated. Orthopyroxene, clinopyroxene, olivine, Fe–Ti oxides, and apatite are present in various proportions and occur as either single phenocrysts or glomerocrysts (Figs. 3b, c, and 4; Table 2). Glass adheres to all hand-picked phenocrysts analyzed (e.g., Figs. 3d and 4a).

Plagioclase

Plagioclase phenocrysts display euhedral to anhedral morphologies and exhibit zonation patterns including complex and oscillatory zoning (Figs. 3b, 4a, b). The phenocrysts range in composition from An_{28} to An_{90} (Fig. 5; Table 3).

Plagioclase phenocrysts from the 1991 basalt range in composition from An_{46} to An_{80} (Fig. 5; Table 3). Phenocrysts display both complex and oscillatory zoning and evidence for partial resorption (i.e., embayments and dissolution zones) and sieve textures are common (Figs. 4a, b). Core compositions cover a large range (An_{30} to An_{87}), with a distinct peak in the data centered on An_{75} . Plagioclase phenocryst rims from the 1991 basalt occupy a narrower compositional range (An_{46} to An_{77}) with two distinct peaks, one at An_{58} and the other at An_{75} (Kratzmann et al. 2009). Some of the 1991 basalt plagioclase rim and core compositions are similar to the averaged 1991 trachyandesite anorthite value (Kratzmann et al. 2009). Phenocryst compositions from the 1991 trachyandesite eruption range from An_{28} to An_{70} (Fig. 5; Table 3). Including the rim and core compositions extends the range to An_{83} , with the majority of both rim and core compositions clustering around An_{43} (Kratzmann et al. 2009). The average 1991 trachyandesite plagioclase composition (An_{43}) is more similar to the 1991 basalt rim average (An_{58}) than to the average 1991 basalt (An_{68}) phenocrysts (Kratzmann et al. 2009).

The 3600 plagioclase phenocrysts occupy a much narrower range in composition (An_{31} to An_{41}) relative to the 1991 trachyandesite and 6700 products (Fig. 5; Table 3). Both the core and rim compositions cover a limited range (An_{31} to An_{42}), with a distinct peak at about An_{36} . There are no apparent compositional trends within subunits (A, B, or C) in the samples analyzed (Fig. 5).

Plagioclase phenocrysts from the 6700 eruption range in composition from An_{36} to An_{88} (Fig. 5; Table 3). The majority of both rim and core compositions cluster around

Fig. 3 Photomicrographs of samples from all three Holocene eruptions, 1991 (**a** and **b**), 3600 (**c** and **d**), and 6700 (**e–h**).

a 1991 pumice sample (HUD207) showing glass (*gl*), vesicles (*v*) and infilling fine ash. Field of view (FOV) 2 mm.

b Representative phenocryst assemblage including zoned and embayed subhedral plagioclase (*pl*), euhedral pyroxene (*px*) and Fe–Ti oxides (*oxides*) (HUD210). FOV ~2 mm.

c Glomerocryst from 3600 pumice sample (HUD202) with euhedral and subhedral plagioclase (*pl*), subhedral to anhedral pyroxene (*px*), apatite and Fe–Ti oxides (FOV ~4 mm).

d Grain mount sample showing glass attached to euhedral plagioclase phenocryst. Note laser ablation spots in glass, melt inclusions (*mi*), and grain mounting medium. FOV ~2 mm.

e Pumice sample from the 6700 event (HUD205), FOV ~4 mm. Note the slightly darker region in the center of the image with more elongated or stretched vesicles relative to the more ovoid shapes of the surrounding paler colored glass.

f Close-up of the gray boxed area from image **e**. The elongated vesicles (*darker glass*) appear to transition into the finely vesiculated pale glass (*arrow*), FOV ~1.5 mm. Plane polarized (**g**) and crossed polarized (**h**) photomicrographs of a xenocryst from the 6700 event (HUD212). Note the vesicular nature of the pumice surrounding the microlite-rich xenocryst (FOV ~4 mm)

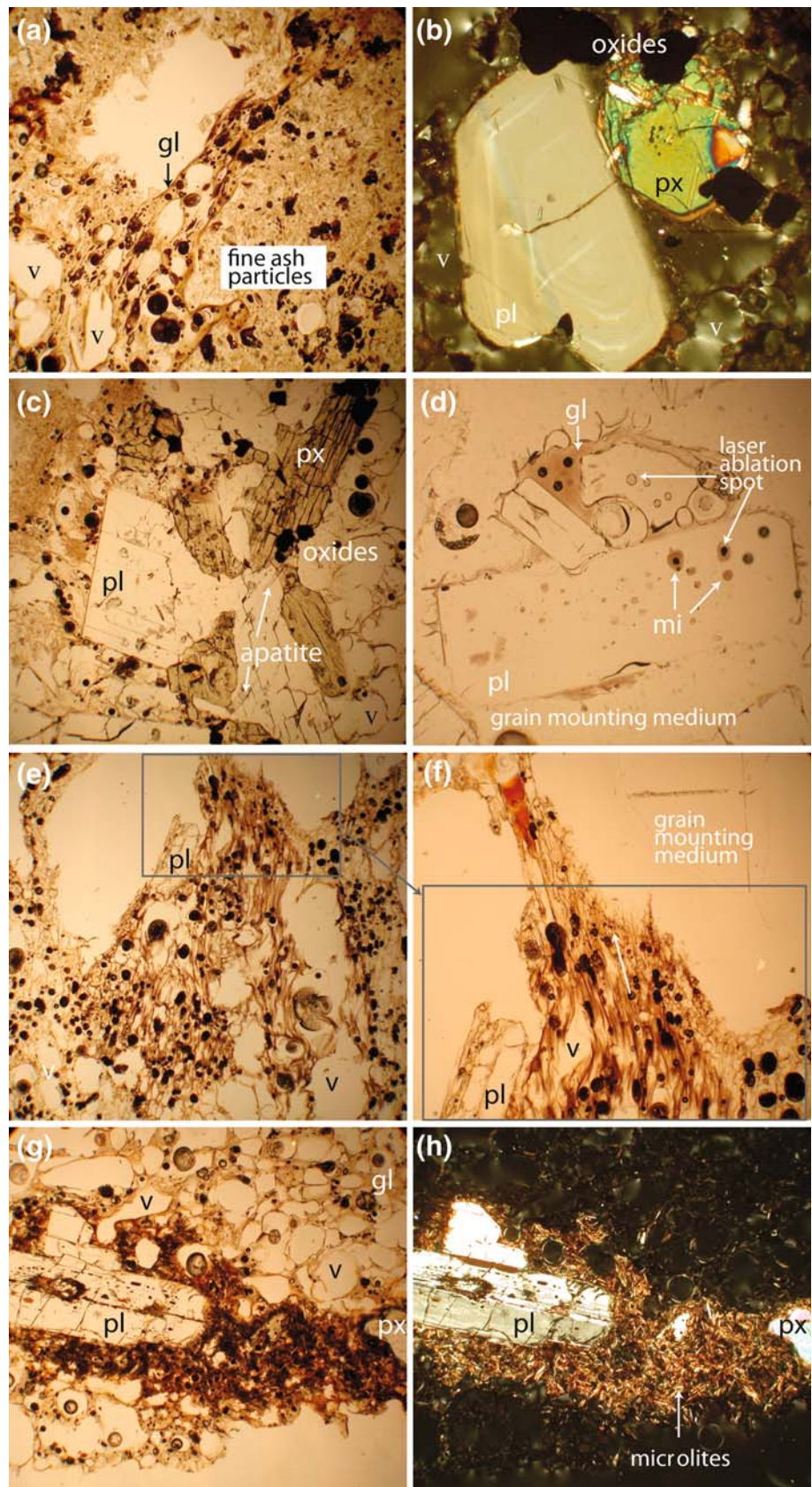


Fig. 4 Backscattered electron (BSE) images of juvenile pyroclasts from the Holocene eruptions. **a** Euhedral plagioclase phenocryst from phase 1 of the 1991 eruption with a more sodic core (An_{31}), a dissolution zone, and a more calcic rim (An_{58}). **b** Close-up of the dissolution zone. **c** and **d** Representative examples of phenocrysts from phase 2 of the 1991 eruption. Compare the microlite-poor glass (**c**; sample HUD209) with the microlite-rich glass (**d**; sample HUD210) adhered to the crystals. **e** Anhedral plagioclase and subhedral magnetite and ilmenite from the 3600 event (HUD204). **f** Xenocryst from the 6700 event (refer to Fig. 3g, h)

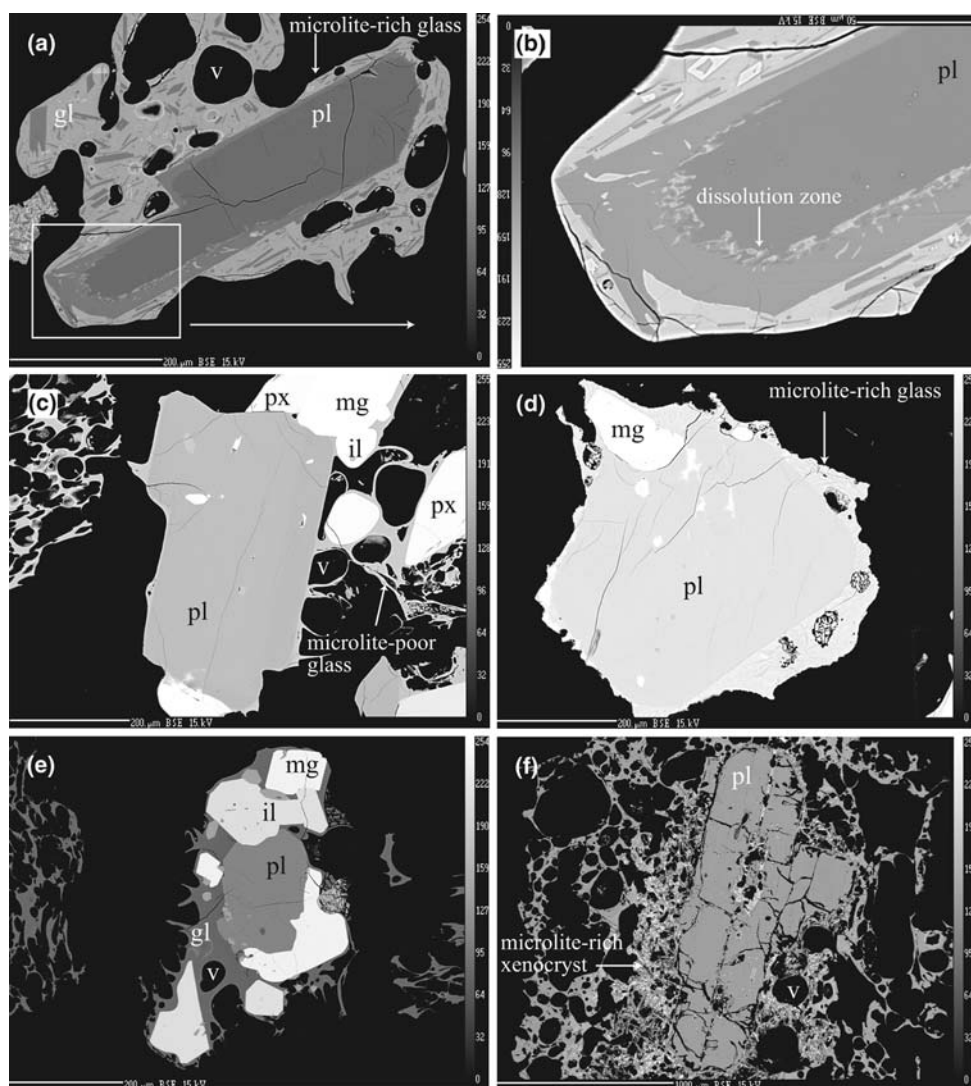


Table 2 Phenocryst assemblages for the Holocene eruptions at Hudson volcano

Eruption	Phase	Unit	Crystallinity	Phenocryst assemblage							$\sum r^2$	n
				Plag	Opx	Cpx	Ol	Mag	Ilm	Apa		
1991	P1 ^a		1.2–2.2	0.6–1.3	0.4–0.5	–	0.4–0.5	<0.1	0.2–0.3	<0.1–0.1	0.014–0.019	3
1991	P2	D	6.1–9.0	4.7–7.0	–	0.5–1.1	<0.1–0.1	0.9–1.1	–	–	0.230–0.265	2
		C	8.6–10.3	6.7–8.0	–	–	0.1–0.4	1.8–1.9	–	–	0.090–0.107	3
		B	10.2–14.5	7.0–10.5	–	0.8–1.3	0.2–1.0	1.7–2.0	–	–	0.036–0.099	4
		A	9.5–15.6	6.6–10.7	–	1.0–2.0	0.4–0.7	1.5–2.4	–	–	0.016–0.108	6
		C	25.7–27.7	22.9–24.3	1.0	–	–	2.4–2.6	0.2–0.3	–	1.220–1.280	2
3600		B	19.7–22.0	16.4–18.5	1.5–1.6	–	–	1.8–1.9	0.1–0.3	–	0.370–0.747	3
		A	22.4–23.5	17.5–18.7	2.5–2.6	–	–	0.2–0.6	1.7–2.0	–	0.297–0.495	2
6700		B	21.5–27.0	16.6–20.9	3.1–3.5	–	–	0.7–1.3	0.6–0.8	0.6–0.7	0.060–0.078	3
		A	15.6–21.2	11.0–15.1	1.1–2.6	0.1–0.3	–	1.1–1.6	0.2–0.4	0.3–0.6	0.056–0.164	6

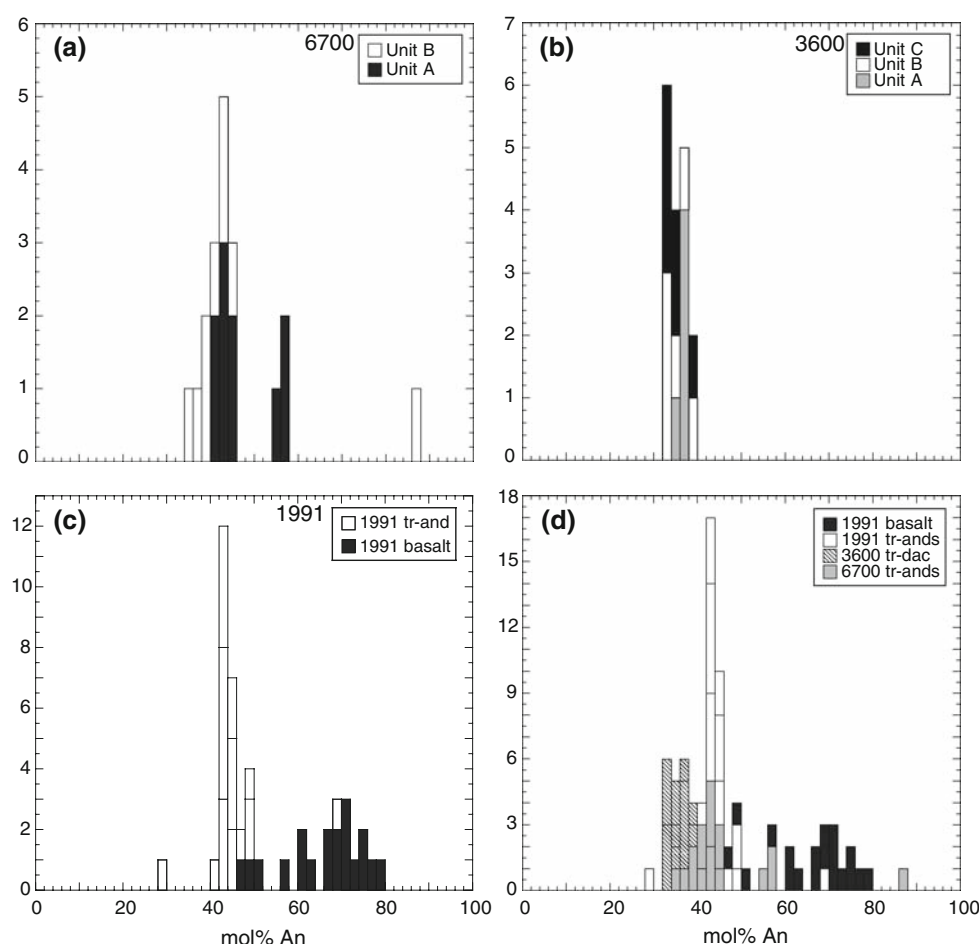
Range in crystallinities calculated using bulk rock data (via Igpet).

Plag plagioclase, Opx orthopyroxene, Cpx clinopyroxene, Ol olivine, Apa apatite, $\sum r^2$ sum of squares of residuals, n number of analyses

^a Calculated using bulk rock data from Ippach (2001, unpublished thesis)

Fig. 5 Histograms showing the distribution of anorthite values for plagioclase phenocrysts from the Hudson eruptions.

a 6700 compositions from ~19 phenocrysts taken from three samples (HUD212, HUD205 and HUD187). **b** 3600 compositions from ~17 phenocrysts taken from three samples (HUD202, HUD203 and HUD204). **c** 1991 compositions. 1991 basalt from 19 phenocrysts taken from 2 samples (HUD110-2 and HUD110-3), and 1991 trachyandesite compositions from ~26 phenocrysts taken from four samples (HUD207, HUD208, HUD209 and HUD210). **d** All data plotted for comparison. Note the highly calcic values for two samples from the 1991 and 6700 trachyandesite eruptions



An₄₁. Sample HUD212 has an average plagioclase composition of An₈₈ that is more similar to the 1991 basalt values (up to An₈₀). There are no apparent compositional trends within subunits (Fig. 5).

Ferro-magnesian minerals

Clino- and orthopyroxene typically occur as euhedral to subhedral phenocrysts either as individual grains or as glomerocrysts. Clinopyroxene is present in the 1991 trachyandesite samples and in trace amounts in the 6700 samples, but not in the 1991 basalt or the 3600 products. Orthopyroxene is found in all samples with the exception of the 1991 trachyandesite, where olivine is present in small amounts (Table 2). The compositional range occupied by the phenocrysts is very narrow with clinopyroxenes clustering around Wo_{~42}En_{~43}Fs_{~15} and orthopyroxenes at Wo_{~3}En_{~68}Fs_{~29} (Table 4). Most phenocrysts are relatively homogeneous, with no core-to-rim variations. Subhedral to anhedral olivine (Fo_{~68} 1σ = 0.3) is present in the 1991 basalt and small amounts in the 1991 trachyandesite (Tables 2, 4).

In general, the Fe–Ti oxides are subhedral to anhedral and some phenocrysts are highly fractured (Figs. 4c–e). They occur as clusters of large magnetite and smaller ilmenite crystals with visible resorption textures. No core-to-rim compositional variations were identified within the oxides analyzed (Table 5).

Matrix glass compositions

The compositional variation in matrix glasses from the least evolved 1991 basalt to the most evolved 3600 trachydacite display slightly curvilinear trends on bivariate element-silica diagrams defined by decreasing MgO, FeO, CaO, TiO₂ and P₂O₅, and increasing K₂O and Na₂O (Fig. 6; Table 6). Distinct gaps in the trend occur from ~54 to 60 and 65 to 68 wt% SiO₂.

The 1991 glasses are more diverse in composition than those from both the 3600 and 6700 eruptions, and range from basalt to trachydacite. Glasses from the initial phase of the 1991 eruption occupy a narrow compositional range from basalt to basaltic trachyandesite (50–54 wt% SiO₂). The 1991 paroxysmal phase matrix glasses occupy a

Table 3 Representative electron microprobe analyses of plagioclase phenocrysts rims and cores from the three major Holocene Hudson eruptions

Eruption	Phase	Unit	Sample	SiO ₂	Al ₂ O ₃	FeO	CaO	Na ₂ O	K ₂ O	Total	An	Ab	Or	Comment
1991	P1		HUD110	51.27	31.15	0.63	13.87	3.44	0.12	100.48	68.81	29.11	0.71	Rim
			HUD110	47.41	33.60	0.53	17.16	1.84	0.05	100.59	83.27	14.97	0.30	Core
			HUD110	53.45	29.00	0.85	11.83	4.41	0.20	99.75	58.69	37.32	1.18	Rim
			HUD110	61.00	24.84	0.33	6.26	7.36	0.52	100.30	31.06	62.28	3.07	Core
1991	P2	D	HUD210	54.97	28.34	0.91	11.15	4.80	0.22	100.39	55.13	40.62	1.30	Rim
			HUD210	47.46	33.51	0.54	17.01	1.86	0.05	100.42	82.94	15.59	0.30	Core
		C	HUD207	57.25	27.12	0.56	9.41	5.66	0.30	100.31	46.68	47.89	1.77	Rim
			HUD207	55.95	28.16	0.53	10.20	5.32	0.25	100.41	50.60	45.02	1.48	Core
		B	HUD208	57.44	27.16	0.54	8.88	5.95	0.31	100.27	44.05	50.35	1.83	Rim
			HUD208	57.59	26.58	0.43	8.53	6.09	0.33	99.55	42.32	51.53	1.95	Core
		A	HUD209	57.56	26.83	0.54	8.68	5.99	0.32	99.93	43.06	50.69	1.89	Rim
			HUD209	59.16	25.85	0.44	7.51	6.56	0.39	99.90	37.26	55.51	2.30	Core
		C	HUD202	60.48	25.49	0.50	6.92	6.74	0.53	100.66	35.06	61.76	3.18	Rim
			HUD202	59.16	25.80	0.50	7.58	6.37	0.46	99.87	38.56	58.62	2.10	Core
3600		B	HUD203	60.34	24.57	0.51	6.09	6.94	0.56	99.01	31.52	65.00	3.47	Rim
			HUD203	59.25	25.32	0.48	7.03	6.61	0.50	99.18	35.92	61.06	2.50	Core
		A	HUD204	60.00	25.35	0.50	6.82	6.83	0.50	100.00	34.49	62.52	3.00	Rim
			HUD204	59.83	25.58	0.45	6.98	6.68	0.51	100.04	35.46	61.44	2.24	Core
		B	HUD205	59.61	25.48	0.55	7.09	6.79	0.46	99.98	35.57	61.65	2.77	Rim
			HUD205	59.77	25.47	0.49	7.14	6.64	0.46	99.98	36.23	60.96	2.80	Core
		B	HUD212	47.24	34.27	0.68	17.42	1.57	0.04	101.22	85.81	13.97	0.23	Rim
			HUD212	46.16	34.71	0.60	18.22	1.25	0.02	100.95	88.84	11.04	0.11	Core
		A	HUD187	57.64	26.67	0.56	8.89	5.88	0.31	99.96	44.65	53.48	1.87	Rim
			HUD187	57.17	26.82	0.50	8.68	5.92	0.34	99.43	43.84	54.12	2.04	Core

An anorthite, Ab albite, Or orthoclase

slightly broader compositional range (60–65 wt% SiO₂) encompassing trachyandesite to trachydacite (Table 6). Within the 1991 paroxysmal phase glasses there exists a systematic progression in composition from trachydacitic early in the sequence to trachyandesitic at the end of the eruption (Kratzmann et al. 2009).

More evolved, compositionally homogeneous trachydacite was erupted during the 3600 event (Fig. 6; Table 6). Glasses occupy a very narrow compositional range (68–70 wt% SiO₂) with no internal compositional variations identified within the sampled stratigraphy.

The melt phase of the 6700 eruption was trachyandesite, with some compositional diversity towards trachydacite, but generally less evolved than the 3600 magma (Fig. 6; Table 6). Glasses occupy a relatively narrow SiO₂ range (62–65 wt%), and unlike the 1991 trachyandesite there are no systematic compositional variations as a function of stratigraphic level. The field defined by the 6700 glasses overlaps the more evolved end of the 1991 trachyandesite compositional spectrum (Fig. 6).

Melt inclusion compositions

Light to dark brown, plagioclase- and pyroxene-hosted melt inclusions are common in the products from the three eruptions investigated. No significant compositional variations were found between plagioclase or pyroxene host crystals.

The 1991 basalt–andesite melt inclusions encompass a relatively narrow compositional range (53–57 wt% SiO₂), and are typically more evolved than the surrounding matrix glass (Fig. 7a; Table 7). Melt inclusions from the paroxysmal phase of the 1991 eruption occupy a narrow SiO₂ range (62–65 wt%), and in general they are either similar to, or more evolved than their co-existing matrix glasses (Fig. 7b; Table 7). As the 1991 eruption progressed, there is a trend in the range of the analyzed matrix glass extending to more mafic compositions relative to the coexisting melt inclusions (Kratzmann et al. 2009).

Melt inclusions from the 3600 eruption are compositionally homogeneous and occupy a narrow SiO₂ range

Table 4 Representative electron microprobe analyses of pyroxene and olivine phenocrysts from the Holocene eruptions of Hudson volcano

Eruption	Phase	Unit	Sample	SiO ₂	TiO ₂	Al ₂ O ₃	FeO	MnO	MgO	CaO	Na ₂ O	K ₂ O	Cr ₂ O ₃	Total	En	Wo	Fs	Fo	Fa
1991	P1		HUD110C-2 cpx	51.53	0.84	2.25	7.71	0.36	15.79	20.37	0.33	0.003	0.001	99.19	45.4	42.1	12.5	–	–
			HUD110C-3 opx	50.60	0.63	0.67	17.64	1.18	24.05	1.68	0.03	0.001	0.014	96.23	68.6	3.4	28.0	–	–
			HUD110C-5 ol	36.15	0.05	0.01	27.59	1.02	33.35	0.20	0.01	0.010	0.002	98.39	–	–	–	68.3	31.7
1991	P2	D	HUD210A-1 cpx	50.71	0.97	2.66	8.79	0.58	15.13	19.79	0.42	0.010	0.008	99.07	44.1	41.5	14.4	–	–
			HUD210A-3 ol	37.03	0.04	0.03	27.62	1.05	33.55	0.14	0.02	0.040	0.014	99.53	–	–	–	68.4	31.6
		C	HUD207D-1 cpx	51.96	0.77	1.91	8.65	0.61	15.29	20.29	0.43	0.004	0.001	99.91	44.0	42.0	14.0	–	–
			HUD207C-3 ol	37.10	0.02	0.02	27.39	1.04	33.36	0.16	0.00	0.011	0.002	99.09	–	–	–	68.5	31.5
		B	HUD208A-1 cpx	51.77	0.74	1.91	8.79	0.62	15.29	20.09	0.46	0.003	0.000	99.22	44.1	41.7	14.2	–	–
			HUD208A-3 ol	37.25	0.02	0.01	27.79	1.09	33.29	0.16	0.01	0.009	0.000	99.63	–	–	–	68.1	31.9
		A	HUD209B-1 cpx	51.58	0.79	2.08	8.68	0.55	15.44	20.21	0.44	0.012	0.007	99.78	44.3	41.7	14.0	–	–
			HUD209B-2 ol	37.32	0.04	0.04	27.72	1.04	33.68	0.17	0.02	0.014	0.020	100.08	–	–	–	68.4	31.6
		C	HUD202A-3 opx	53.84	0.31	0.64	18.01	1.22	24.38	1.56	0.05	0.009	0.001	100.03	68.5	3.2	28.4	–	–
			HUD202A-1 cpx	51.60	0.66	1.78	9.29	0.74	14.48	20.23	0.46	0.009	0.001	99.25	42.3	42.5	15.2	–	–
3600		B	HUD203A-1 opx	53.13	0.31	0.64	18.09	1.24	23.94	1.50	0.02	0.004	0.003	98.87	68.1	3.1	28.9	–	–
			HUD203A-2 cpx	51.50	0.65	1.73	8.98	0.67	15.03	19.96	0.40	0.007	0.003	98.94	43.7	41.7	14.6	–	–
		A	HUD204A-1 opx	53.36	0.30	0.64	18.61	1.31	23.87	1.50	0.09	0.005	0.004	99.70	67.5	3.1	29.5	–	–
			HUD204A-2 cpx	52.29	0.51	1.45	9.40	0.77	14.94	19.90	0.48	0.030	0.002	99.76	43.3	41.4	15.3	–	–
		B	HUD212C-4 opx	53.50	0.40	0.99	16.94	0.87	25.25	1.81	0.04	0.004	0.014	99.83	70.0	3.6	26.4	–	–
			HUD212C-5 cpx	52.14	0.72	1.67	8.85	0.61	15.52	19.74	0.43	0.016	0.008	99.71	44.8	40.9	14.3	–	–
		B	HUD205B-4 opx	53.99	0.36	0.69	16.30	1.00	25.59	1.75	0.06	0.004	0.003	99.74	71.1	3.5	25.4	–	–
			HUD205B-1 cpx	51.67	0.79	1.93	9.25	0.60	15.29	19.76	0.45	0.008	0.004	99.76	44.1	41.0	15.0	–	–
		A	HUD187A-1 opx	53.61	0.45	0.89	17.37	1.06	24.65	1.75	0.07	0.002	0.008	99.86	69.1	3.5	27.3	–	–
			HUD187A-2 cpx	51.82	0.77	1.80	9.14	0.60	15.49	19.71	0.47	0.003	0.006	99.82	44.5	40.7	14.7	–	–

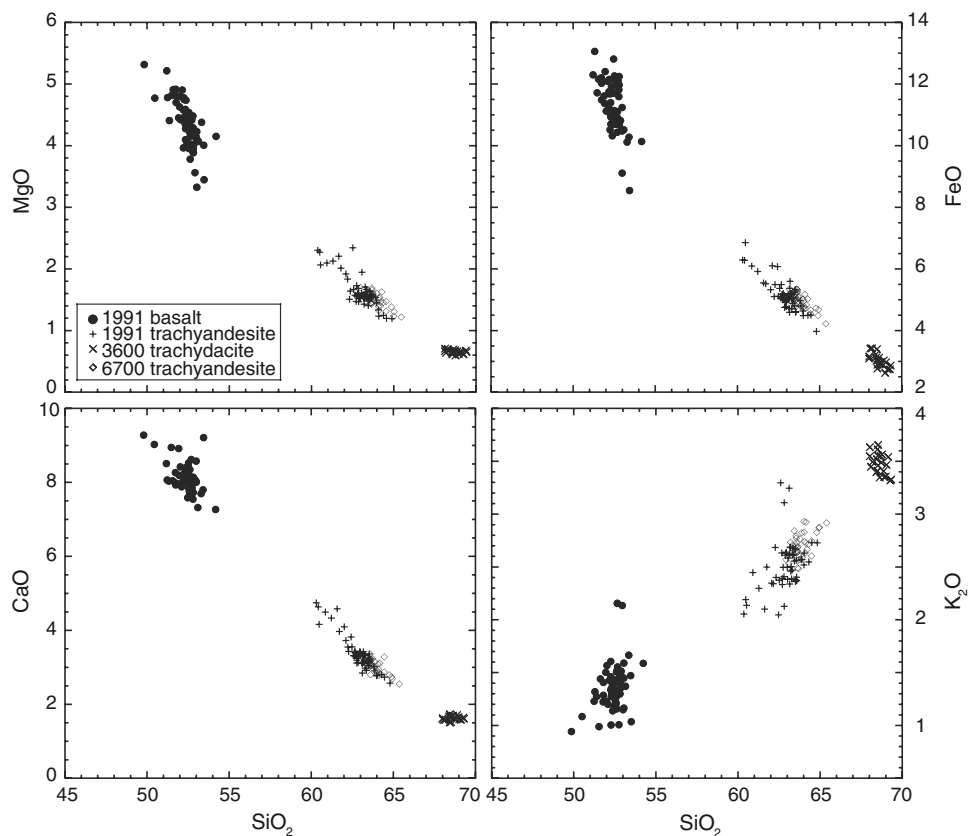
cpx clinopyroxene, opx orthopyroxene, ol olivine, En enstatite, Wo wollastonite, Fs ferrosilite, Fo forsterite, Fa fayalite

Table 5 Representative electron microprobe analyses of Fe–Ti oxide pairs from the Holocene eruptions of Hudson volcano

Eruption	Phase	Unit	Sample	TiO ₂	Al ₂ O ₃	FeO	MnO	MgO	Cr ₂ O ₃	Total	Usp (mol%)	Ilm (mol%)
1991	1		HUD110-1	19.18	1.54	71.94	0.58	0.75	0.09	94.07	43.9	–
			HUD110-1	49.47	0.10	45.25	0.80	1.47	0.01	97.10	–	86.7
1991	2	D	HUD210-2	15.63	2.74	72.37	0.87	3.79	0.01	95.42	44.1	–
			HUD210-2	45.05	0.39	45.21	0.86	4.95	0.01	96.47	–	83.1
		C	HUD207-1	15.68	2.79	72.28	0.82	3.75	0.02	95.34	44.5	–
			HUD207-1	45.23	0.36	45.23	0.82	5.26	0.01	96.91	–	82.7
		B	HUD208-2	15.79	2.89	72.10	0.79	3.80	0.02	95.40	45.2	–
			HUD208-2	45.24	0.34	45.25	0.88	4.73	0.01	96.45	–	83.0
		A	HUD209-2	15.65	2.79	72.41	0.86	3.75	0.02	95.49	44.3	–
			HUD209-2	44.80	0.34	45.23	0.93	5.28	0.01	96.59	–	82.0
		C	HUD202-1	14.51	2.09	76.06	0.95	2.67	0.03	96.31	40.6	–
			HUD202-1	45.04	0.26	47.53	1.08	3.97	0.01	97.89	–	82.7
3600		B	HUD203-1	14.21	2.06	75.52	1.01	2.61	0.02	95.44	40.1	–
			HUD203-1	44.35	0.31	47.58	1.11	3.88	0.02	97.25	–	81.9
		A	HUD204-1	14.30	2.02	76.01	0.98	2.65	0.03	96.00	40.0	–
			HUD204-1	44.65	0.24	47.51	1.13	3.81	0.02	97.35	–	82.5
		B	HUD205-3	14.88	2.91	73.71	0.81	3.66	0.05	96.03	42.0	–
			HUD205-3	43.49	0.40	47.39	0.70	4.82	0.01	96.82	–	79.5
		B	HUD212-2	15.60	2.47	73.27	0.83	3.50	0.03	95.71	43.8	–
			HUD212-2	44.68	0.34	45.87	0.83	4.81	0.01	96.55	–	82.3
		A	HUD187-1	14.73	2.93	72.71	0.72	3.99	0.05	95.13	41.5	–
			HUD187-1	44.08	0.38	46.75	0.74	4.95	0.01	96.92	–	80.5

mol% mole percent, Usp ulvöspinel, Ilm ilmenite

Fig. 6 Representative major element variation diagrams of matrix glass from the Holocene explosive eruptions at Hudson volcano. Note the compositional gap between ~55 and ~60 wt% SiO₂. Additional averaged major element data are available in Table 6. Number of analyses (n): 1991 basalt, n = 36; 1991 trachyandesite, n = 54; 3600, n = 15; 6700, n = 41. Symbols as per Fig. 2. All data normalized to 100 prior to plotting



(67–69 wt%). There are no systematic compositional variations within the 3600 stratigraphy, and in general there is considerable overlap of the melt inclusions and coexisting matrix glasses (Fig. 7d; Table 7).

Melt inclusions from the 6700 eruption occupy a broader compositional range than their coexisting matrix glasses (63–67 wt% SiO₂) (Fig. 7c; Table 7). There appear to be two distinct populations within the 6700 melt inclusion data that are linked to different stratigraphic units (not shown). Unit A (sample HUD187; base of the stratigraphy) melt inclusions encompass a narrow compositional range (63–65 wt% SiO₂) compared to the range occupied by Unit B samples (HUD205 and HUD212; top of the stratigraphy) (63–67 wt% SiO₂).

Trace element data

Hudson magmas typically have elevated incompatible elements (i.e., LILE, HFSE and REE) relative to other SVZ calc-alkaline rocks (e.g., Gutiérrez et al. 2005). In general, the incompatible trace element concentrations increase with increasing SiO₂ content. An enrichment in select trace elements (e.g., Zr) occurs within the 3600 and 6700 glasses relative to the 1991 trachyandesite glasses (Fig. 8).

Chondrite-normalized rare-Earth element plots from all eruptions have similar, LREE-enriched trends. The

trachyandesite and trachydacite compositions have higher concentrations of REE relative to the 1991 basalt (Fig. 9; Supplementary Table S1) and the degree of LREE enrichment increases in the more evolved compositions. Negative Eu anomalies are present in all REE patterns and represent varying degrees of plagioclase fractionation. The anomaly is more pronounced in the evolved compositions than in the 1991 basalt and reflects the greater crystallinity seen in these samples (~25 vs. ~2%). The REE patterns are similar to previously published work (e.g., López-Escobar et al. 1993; Gutiérrez et al. 2005).

The Hudson samples show an increase in La/Yb and a decrease in Dy/Yb with increasing degree of differentiation (Fig. 10), but no apparent trends in Ce/Yb versus Yb. These particular trace element ratios have been identified as potential indicators for the depth of differentiation (e.g., Feeley and Davidson 1994; Macpherson et al. 2006; Davidson et al. 2007). All samples show a Nb anomaly typical of subduction zone environments (Wilson 1989) when plotted on a Rock/MORB normalized 'spider' diagram.

Pre-eruptive intensive parameters

Hudson volcano has been one of the most active centers in southern South America during the Holocene, yet little is

Table 6 Averaged matrix glass compositions from the major Holocene eruptions of Hudson volcano as measured by electron microprobe

Eruption	1991							
Phase	P1				P2			
Unit	—				A		B	
Sample Glass	HUD110 trans	HUD110 trans	HUD110 trans	HUD110 tachy	HUD209 trans	HUD209 trans	HUD208 trans	HUD208 trans
SiO ₂	52.55 (0.15)	52.52 (0.23)	51.68 (0.19)	52.27 (0.32)	62.76 (0.30)	64.10 (1.01)	62.23 (0.35)	63.06 (0.46)
TiO ₂	2.58 (0.03)	2.22 (0.08)	2.33 (0.03)	2.23 (0.16)	1.22 (0.07)	1.09 (0.04)	1.21 (0.09)	1.20 (0.09)
Al ₂ O ₃	13.93 (0.14)	15.79 (0.20)	15.47 (0.25)	15.18 (0.58)	16.10 (0.18)	16.33 (0.03)	16.18 (0.20)	16.20 (0.05)
FeO	12.16 (0.37)	10.72 (0.15)	11.33 (0.12)	10.88 (0.68)	4.69 (0.19)	4.59 (0.55)	4.94 (0.16)	4.99 (0.10)
MnO	0.23 (0.08)	0.20 (0.07)	0.17 (0.01)	0.13 (0.03)	0.18 (0.05)	0.21 (0.06)	0.18 (0.07)	0.18 (0.05)
MgO	3.99 (0.08)	4.28 (0.12)	4.46 (0.10)	4.39 (0.44)	1.52 (0.02)	1.41 (0.20)	1.58 (0.07)	1.45 (0.06)
CaO	7.72 (0.09)	8.20 (0.15)	8.41 (0.17)	8.27 (0.64)	3.24 (0.08)	2.91 (0.28)	3.32 (0.17)	3.22 (0.26)
Na ₂ O	4.24 (0.16)	4.28 (0.23)	3.93 (0.07)	4.12 (0.14)	6.70 (0.27)	6.68 (0.22)	6.64 (0.16)	6.74 (0.26)
K ₂ O	1.45 (0.06)	1.23 (0.08)	1.30 (0.01)	1.22 (0.22)	2.57 (0.13)	2.68 (0.06)	2.40 (0.06)	2.62 (0.06)
P ₂ O ₅	0.88 (0.05)	0.70 (0.07)	0.93 (0.01)	0.78 (0.04)	0.35 (0.04)	0.35 (0.04)	0.36 (0.06)	0.39 (0.02)
Total	99.72 (0.38)	100.15 (0.16)	99.07 (0.01)	99.47 (0.93)	99.33 (0.32)	100.01 (0.33)	99.04 (0.52)	99.67 (0.13)
<i>n</i>	6	5	3	3	8	3	5	3

Eruption	1991			3600			6700	
Phase	P2			—			—	
Unit	C	D		A	B	C	B	A
Sample Glass	HUD207 trans	HUD210 trans	HUD210 tachy	HUD202 trans	HUD203 trans	HUD204 trans	HUD212 trans	HUD187 trans
SiO ₂	61.59 (0.96)	62.42 (0.47)	60.84 (0.39)	67.93 (0.38)	67.23 (0.39)	68.49 (0.30)	64.24 (0.43)	63.10 (0.77)
TiO ₂	1.31 (0.07)	1.27 (0.06)	1.47 (0.02)	0.60 (0.08)	0.63 (0.06)	0.68 (0.02)	1.21 (0.04)	1.35 (0.08)
Al ₂ O ₃	16.01 (0.08)	15.97 (0.13)	15.75 (0.21)	15.14 (0.16)	15.11 (0.21)	15.34 (0.08)	15.29 (0.22)	15.69 (0.18)
FeO	5.49 (0.49)	5.23 (0.08)	6.18 (0.48)	3.05 (0.23)	3.00 (0.28)	3.05 (0.11)	4.41 (0.19)	4.98 (0.01)
MnO	0.23 (0.05)	0.15 (0.05)	0.22 (0.03)	0.14 (0.03)	0.14 (0.03)	0.11 (0.04)	0.16 (0.05)	0.22 (0.07)
MgO	1.93 (0.24)	1.64 (0.15)	2.15 (0.10)	0.64 (0.03)	0.62 (0.02)	0.64 (0.04)	1.20 (0.02)	1.59 (0.02)
CaO	3.85 (0.54)	3.41 (0.41)	4.50 (0.21)	1.63 (0.08)	1.55 (0.05)	1.67 (0.02)	2.72 (0.06)	3.07 (0.08)
Na ₂ O	6.31 (0.45)	6.16 (0.23)	6.15 (0.08)	6.30 (0.30)	6.44 (0.26)	6.49 (0.12)	6.60 (0.19)	6.34 (0.34)
K ₂ O	2.35 (0.11)	2.99 (0.38)	2.18 (0.15)	3.48 (0.06)	3.43 (0.11)	3.48 (0.10)	2.84 (0.02)	2.65 (0.06)
P ₂ O ₅	0.43 (0.03)	0.42 (0.09)	0.58 (0.04)	0.11 (0.04)	0.10 (0.02)	0.12 (0.04)	0.26 (0.02)	0.38 (0.03)
Total	99.13 (0.35)	99.25 (0.41)	99.44 (0.30)	99.01 (0.60)	98.24 (0.72)	100.07 (0.52)	98.94 (0.54)	99.39 (0.76)
<i>n</i>	6	4	4	4	6	5	3	4

One standard deviation shown in parentheses

n number of analyses, *trans* translucent, *tachy* tachylite

known about the magmatic system beneath the volcano. Kratzmann et al. (2009) recently defined the pre-eruption P/T storage conditions of the trachyandesite magma from the 1991 eruption at approximately 50–100 megapascals (MPa; ~1.5–3 km) and $972 \pm 26^\circ\text{C}$. Mineral geothermometry, volatile component analysis, and comparisons with analog high pressure experiments are used to make similar estimates of storage conditions for the other major Holocene eruptions in order to assess the longer term nature of the magmatic system at Hudson.

Temperatures

Fe–Ti oxide geothermometry (e.g., Andersen and Lindsley 1988) was used to estimate temperatures of equilibration and oxygen fugacities in all three eruptions using the QUILF program (Andersen et al. 1993) (Table 8). Only oxide pairs from the initial phase of the 1991 eruption failed the Bacon and Hirschmann (1988) Mg/Mn equilibrium test, and may reflect phenocryst-melt disequilibrium. Pre-eruptive cooling and degassing of the 1991 basalt is

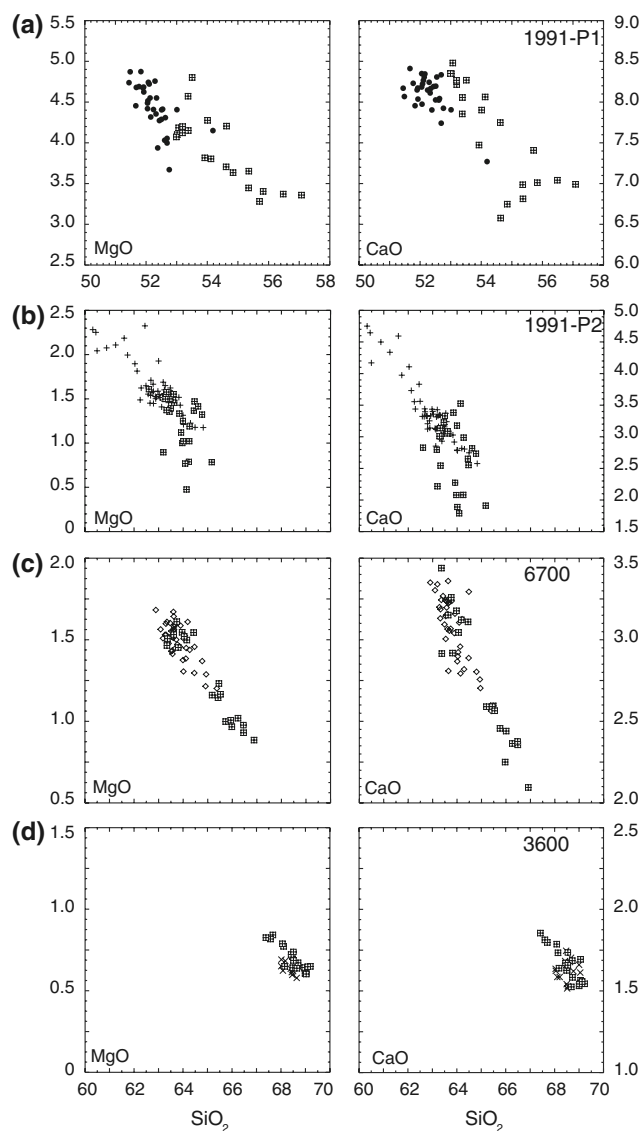


Fig. 7 Representative major element variation diagrams of melt inclusions (*crossed squares*) from the Holocene explosive eruptions at Hudson volcano. Matrix glass (*symbols as per Fig. 2*) plotted for comparison. Additional major element data are available in Table 7. Number of analyses in parentheses: **a** 1991 basalt, melt inclusions (mi) = 22, matrix glass (gl) = 36; **b** 1991 trachyandesite, mi (29), gl (54); **c** 6700, mi (20), gl (41); **d** 3600, mi (21), gl (15). All data normalized to 100 prior to plotting

supported by the emplacement as a lava flow and the numerous microlites identified in many of the pyroclasts (e.g., Taddeucci et al. 2004).

Fe–Ti oxide geothermometry indicates pre-eruptive temperatures for the 6700 eruption ranged from 966 to 979°C (± 25) with an average of $972 \pm 25^\circ\text{C}$ (from 9 oxide pairs). The 3600 temperature range, 934 to 950°C (average $942 \pm 24^\circ\text{C}$), was obtained from analyses of 15 Fe–Ti

Table 7 Compositions of individual melt inclusions from the major Holocene eruptions of Hudson volcano as measured by electron microprobe

Eruption	1991							
Phase	P1				P2			
Unit	—				A	A	B	B
Sample	110-3	110-3	110-2	110-2	209	209	208a	208a
Inclusion	#3	#4	#3	#1	#3	#2	#5	#1
SiO ₂	57.06	53.62	52.05	51.81	61.20	61.89	61.90	63.21
TiO ₂	1.91	2.13	2.09	2.11	1.15	1.17	1.00	0.99
Al ₂ O ₃	16.90	16.49	15.89	15.96	15.40	16.09	15.76	16.09
FeO	8.75	10.06	10.80	10.47	5.77	4.60	5.44	4.33
MnO	0.16	0.24	0.18	0.20	0.22	0.16	0.21	0.19
MgO	3.36	3.79	4.00	4.01	1.45	1.43	1.33	1.32
CaO	6.99	7.43	8.20	8.16	3.11	2.96	3.04	2.78
Na ₂ O	2.82	3.67	3.01	2.95	6.10	5.97	6.12	6.43
K ₂ O	0.97	0.95	1.16	1.23	2.03	2.70	2.59	2.81
P ₂ O ₅	1.03	1.03	0.82	0.81	0.00	0.34	0.34	0.28
Total	99.94	99.40	98.20	97.70	96.44	97.31	97.74	98.44
CO ₂	b.d.l. ^c	b.d.l. ^c	—	—	—	—	—	b.d.l
H ₂ O ^a	0.1 ^c	0.3 ^c	—	—	—	—	—	2.7
H ₂ O ^b	0.06	0.60	1.80	2.30	3.56	2.69	2.26	1.56
Eruption	1991				3600		6700	
Phase	P2				—		—	
Unit	C	D	D	A	B	C	B	B
Sample	207b	210a	210B	204a	203	202	212	205
Inclusion	#2c	#2	#3	#1	#1	#1	#1	#1
SiO ₂	62.76	61.35	62.67	67.33	66.44	66.20	65.62	65.85
TiO ₂	1.28	1.09	1.06	0.71	0.82	0.87	1.08	1.13
Al ₂ O ₃	16.33	16.40	16.16	15.35	15.09	15.10	15.63	15.80
FeO	5.08	4.52	4.50	2.89	3.12	3.28	4.15	3.97
MnO	0.23	0.18	0.17	0.23	0.10	0.14	0.15	0.13
MgO	1.57	1.34	1.31	0.67	0.75	0.82	0.96	1.01
CaO	3.30	2.60	2.87	1.63	1.69	1.76	2.42	2.35
Na ₂ O	6.30	6.35	6.45	5.97	5.97	6.08	6.15	5.75
K ₂ O	2.64	2.93	2.78	3.45	3.45	3.42	3.02	3.14
P ₂ O ₅	0.41	0.30	0.29	0.12	0.11	0.14	0.26	0.29
Total	99.90	97.06	98.27	98.26	97.54	97.81	99.44	99.41
CO ₂	b.d.l	b.d.l	b.d.l	b.d.l	b.d.l	b.d.l	b.d.l	b.d.l
H ₂ O ^a	1.5	2.5	2.9	1.7	2.5	2.2	0.6	0.6
H ₂ O ^b	0.10	2.94	1.73	2.61	2.96	1.94	2.11	1.87

CO₂ was consistently beyond detection limits in melt inclusions analyzed

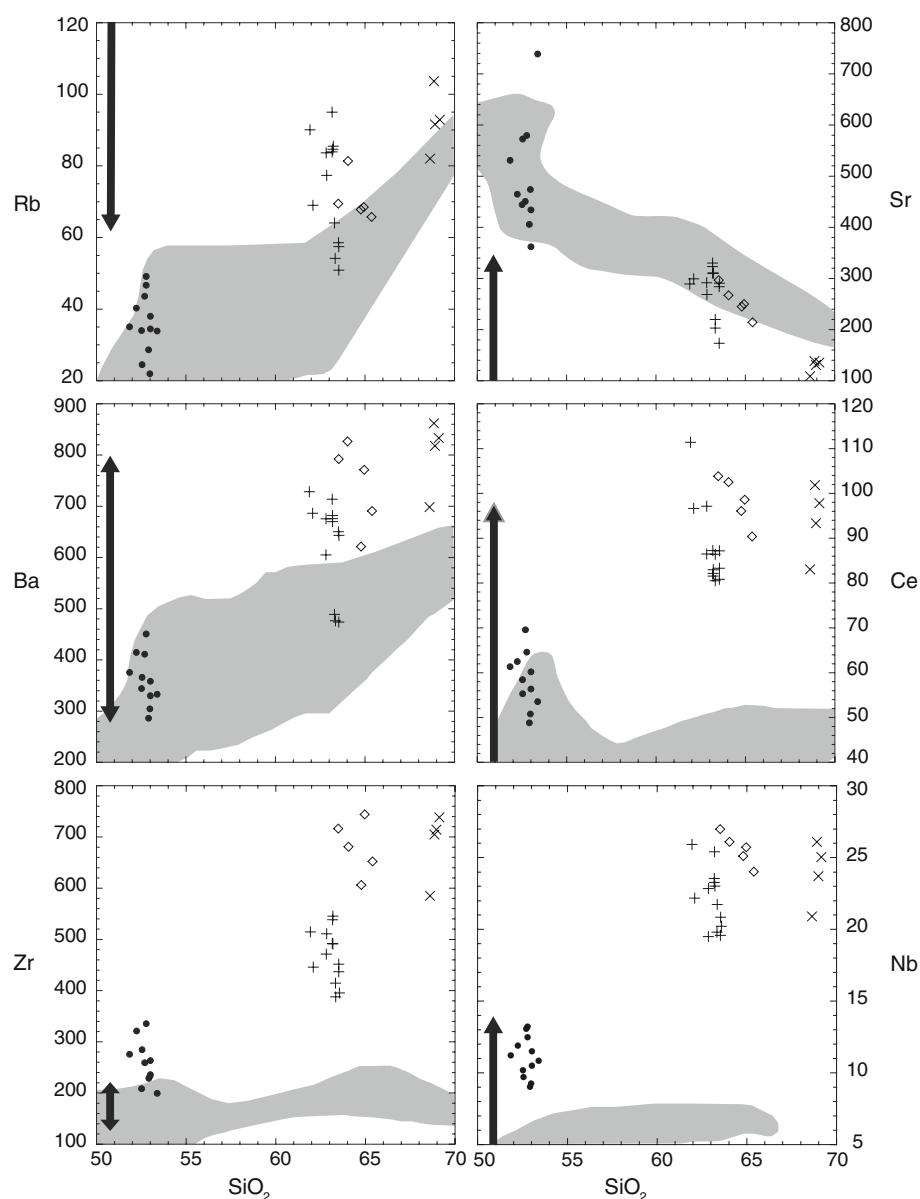
b.d.l beyond detection limits

^a H₂O as measured by FTIR

^b H₂O by WBD method

^c Measured on other samples

Fig. 8 Representative trace element variation diagrams of matrix glasses. *Gray field* range of calc-alkaline rocks from the Southern Volcanic Zone (from Gutiérrez et al. 2005). *Black arrow* range in concentration of the Patagonian Batholith (from Kilian and Behrmann 2003). Number of analyses (*n*): 1991 basalt, *n* = 13; 1991 trachyandesite, *n* = 13; 3600, *n* = 4; 6700, *n* = 5. Symbols as per Fig. 2. SiO₂ data normalized to 100 prior to plotting



oxide pairs. The 1991 trachyandesite temperature range, 970 to 976°C (average $972 \pm 26^\circ\text{C}$; obtained from 17 oxide pairs), is similar to the results obtained for the 6700 eruption. Overall, the estimated temperatures for the evolved magmas occupy a relatively narrow range (934 to 979°C). As the 1991 basaltic samples failed the Mg/Mn equilibrium test, we have used the olivine geothermometers of Roeder and Emslie (1970) and Putirka et al. (2007) to tentatively constrain the temperature range to between 1014–1050°C and 1180–1190°C, respectively.

Oxygen fugacities have been calculated for the three Holocene eruptions being investigated and are typically one log unit above the NNO buffer (Table 8). Oxygen fugacities of magma from the 6700 eruption range from -10.33 to -10.02 (± 0.15), and 3600 from -10.85 to

-10.54 (± 0.16). The 1991 oxygen fugacities range from -10.42 to -10.29 (± 0.17) for the trachyandesite, and from -11.21 to -10.94 (± 0.2) for the basalt.

Volatile content and storage pressures

Water contents in melt inclusions range from 1.8 to 5.3 wt% (Table 8). Both the water by difference method [100-analytical totals (e.g., Anderson 1973; Devine et al. 1995)] and FTIR spectrometry (e.g., Mandeville et al. 2002) were employed, with no apparent correlation between WBD and FTIR values. Given the better precision and accuracy of FTIR compared with WBD (e.g., Devine et al. 1995) we have chosen to use the former in subsequent pressure estimates. Magmatic pressures (assuming water-

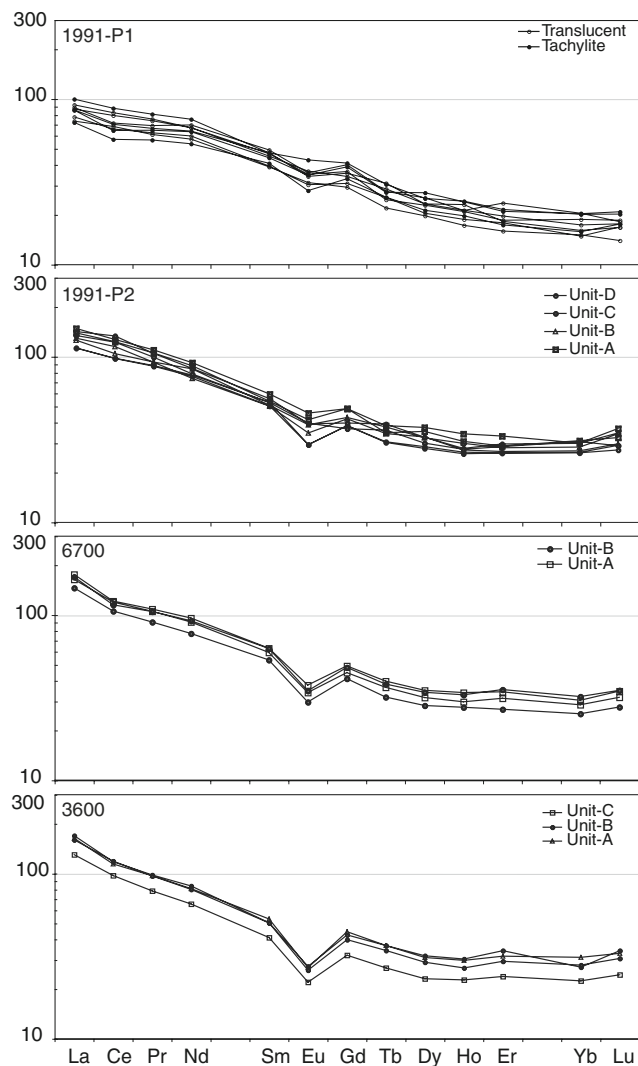


Fig. 9 Chondrite-normalized REE plot for matrix glasses from all three major eruptions. An overall LREE-enriched trend and negative Eu anomaly are visible in all eruptions. The larger Eu anomalies in the older eruptions (3600 and 6700) are due to increases in the degree of plagioclase fractionation (see Table 2)

saturated conditions) were estimated by combining the temperature and FTIR-determined H_2O data with the empirical method for estimating water solubility of Moore et al. (1998). The melt inclusions represent either shallow level trapping of volatile-saturated magma, or deeper level entrapment of volatile under-saturated magma. The calculated pressure ranges are likely to be minimum values based on the evidence for degassing prior to eruption and the assumption of water-saturated conditions. The inferred depths range from 0.2 to 2.7 km (Table 8) and suggest that the relatively evolved magmas produced over the last ~7000 years at Hudson volcano were staged at relatively shallow levels in the crust prior to eruption.

CO_2 concentrations are consistently lower than detection limits (Table 7) in all melt inclusions analyzed. Given

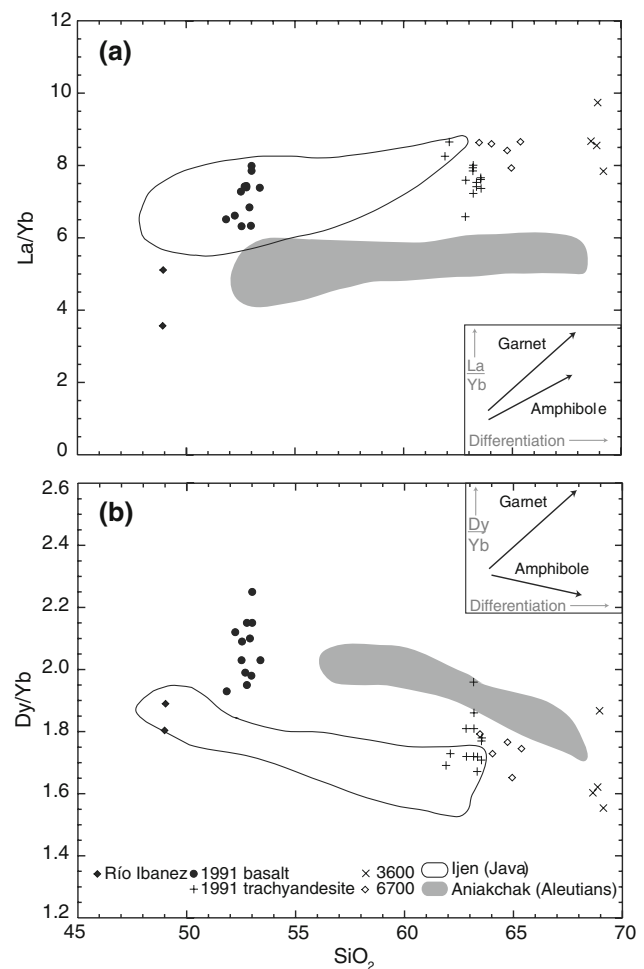


Fig. 10 **a** La/Yb versus SiO_2 . **b** Dy/Yb versus SiO_2 . The Hudson data (this study) mirror the trends seen in other arc settings. Expected garnet and amphibole fraction trends shown in inserts from Davidson et al. (2007). Ijen and Aniakhak data fields from Davidson et al. (2007). SiO_2 data normalized to 100 prior to plotting

that CO_2 can degas almost to completion before H_2O starts to degas [open system degassing (e.g., Dixon and Stolper 1995)] the lack of detectable concentrations indicates a significant level of degassing prior to eruption for all events. The eruption of lava during the initial stage of the 1991 eruption also suggests shallow pre-eruptive degassing of basaltic magma. Further evidence for pre-eruptive degassing of the basaltic melt exists in the widespread microlite development in many of the tephra fragments (e.g., Taddeucci et al. 2004).

Experimental constraints on magma storage

Experimental studies by Luhr (1990) and Moore and Carmichael (1998) have placed important constraints on phase assemblages and melt compositions in crustal magma storage regions of andesitic composition. Tighter constraints on the location of the Holocene magma chambers

Table 8 Pre-eruptive conditions for the Holocene eruptions of Hudson volcano

Eruption	Phase	Unit	Sample	T (°C)	Error	Log f_{O_2}	Error	H ₂ O (weight percent) WBD	H ₂ O (weight percent) FTIR ^a	H ₂ O sol ave km ^b	H ₂ O sol -1 σ	H ₂ O sol +1 σ
1991	P1		HUD110-1	942.6	27.0	-10.94	0.20	–	–	–	–	–
			HUD110-2	927.5	27.3	-11.21	0.21	2.1	0.3 (2)	0.05	0.02	0.09
			HUD110-3	796.0	69.0	-15.63	0.95	–	–	–	–	–
			Average	927.5	27.1	-11.21	0.21	2.1	0.3	0.05	0.02	0.09
1991	P2	D	HUD210	973.5	25.7	-10.30	0.16	4.2	3.2 (7)	2.1	1.6	2.7
		C	HUD207	971.3	25.5	-10.33	0.16	2.6	1.8 (3)	1.2	0.2	2.1
		B	HUD208	969.8	26.5	-10.42	0.18	2.5	1.9 (2)	1.4	0.9	2.0
		A	HUD209	975.7	25.7	-10.29	0.16	4.1	0.8 (1)	1.1	0.5	1.7
			Average	972.5	25.8	-10.33	0.16	3.3	1.9	1.5	0.8	2.1
3600		C	HUD202	943.0	24.0	-10.68	0.16	3.0	2.1 (2)	1.3	1.1	1.4
		B	HUD203	943.6	23.6	-10.63	0.16	–	2.5 (4)	1.6	1.3	2.0
		A	HUD204	939.5	24.0	-10.72	0.16	2.9	2.5 (3)	1.6	1.4	1.8
			Average	942.0	23.9	-10.68	0.16	2.6	2.4	1.5	1.3	1.7
6700		B	HUD212	971.0	25	-10.32	0.16	2.2	1.7 (1)	1.3	1.2	1.4
		B	HUD205	972.6	24.9	-10.22	0.15	–	0.8 (1)	1.1	1.0	1.2
		A	HUD187	972.0	24.0	-10.17	0.14	3.0	–	–	–	–
			Average	972.6	24.9	-10.22	0.15	2.6	1.2	1.2	1.1	1.3

Temperature and oxygen fugacities measured by electron microprobe. The pressures of saturation (expressed as depth in km) are based on FTIR-based water data and have been estimated from the empirical method of Moore et al. (1998)

sol solubility, *std dev* standard deviation, -1σ minus 1 std dev, $+1\sigma$ plus 1 std dev

^a Parentheses contain number of melt inclusions analyzed

^b Based on FTIR data

beneath Hudson volcano can be achieved by comparing experimental work on closely related compositions with the pre-eruptive storage conditions defined in this study. The dominant magma composition for the Holocene explosive eruptions at Hudson volcano is trachyandesite. Potential analogs for the 6700 and 1991 trachyandesite storage conditions include experiments conducted on samples from El Chichón (Luhr 1990), Mt Pelée (Martel et al. 1999) and the Mexican Volcanic Belt (Moore and Carmichael 1998). Possible analogs for the 3600 trachydacite composition include more evolved magmas from Mount St. Helens (Rutherford et al. 1985), Mt Pinatubo (Scailliet and Evans 1999), Santorini (Cottrell et al. 1999), and Volcán San Pedro (Costa et al. 2004).

Phase boundaries for the major mineral phases as defined by experimental work on andesite and trachyandesite compositions (under water-saturated conditions) are shown in Fig. 11a. The temperatures of both the 6700 and the 1991 trachyandesite are well constrained at 972°C (± 25 and ± 26 , respectively). At this temperature the observed mineral assemblage is closely matched by the experimental work of Moore and Carmichael (1998) at pressures up to 200 MPa. The extent of crystallization of the 6700 samples (i.e., 8.5–11.0 vol.%) is similar to the experimentally derived values of Moore and Carmichael (1998) over a relatively large pressure range (up to

180 MPa). The observed mineral assemblage is best matched under 100 MPa and this shallower depth is supported by the narrower depth range (1.0–1.4 km) inferred from melt inclusion data (Table 8). The 1991 trachyandesite crystallinity (9.0–12.0 vol.%) is comparable to the experimental work of Moore and Carmichael (1998) within the pressure range of 120–180 MPa. The lack of amphibole in the natural samples is an important constraint that suggests magma storage at relatively high temperatures and is supported by the experimental work in which amphibole was never found as a stable phase above 970°C irrespective of pressure (Fig. 11). A combination of comparisons to experimental work and petrologic results constrains the trachyandesite pre-eruptive storage conditions to pressures less than 180 MPa, at $\sim 972^\circ\text{C}$ (± 25), and 1–3 wt% H₂O in the melt.

When compared to experimental work on the San Pedro dacite (at 950°C, 2.5–4.0 wt% H₂O in the melt and plagioclase An values; Costa et al. 2004), the Pinatubo dacite (at 950°C, 2.5–3.2 wt% H₂O, the observed mineral assemblage and plagioclase An values; Scailliet and Evans 1999), and the Mt St. Helens dacite (~ 1 –4 wt% H₂O and the observed mineral assemblage; Rutherford et al. 1985), the pre-eruptive storage of the 3600 trachydacite can be constrained to ≤ 200 MPa pressure. The extent of crystallization of the San Pedro (23–50%; Costa et al. 2004) and

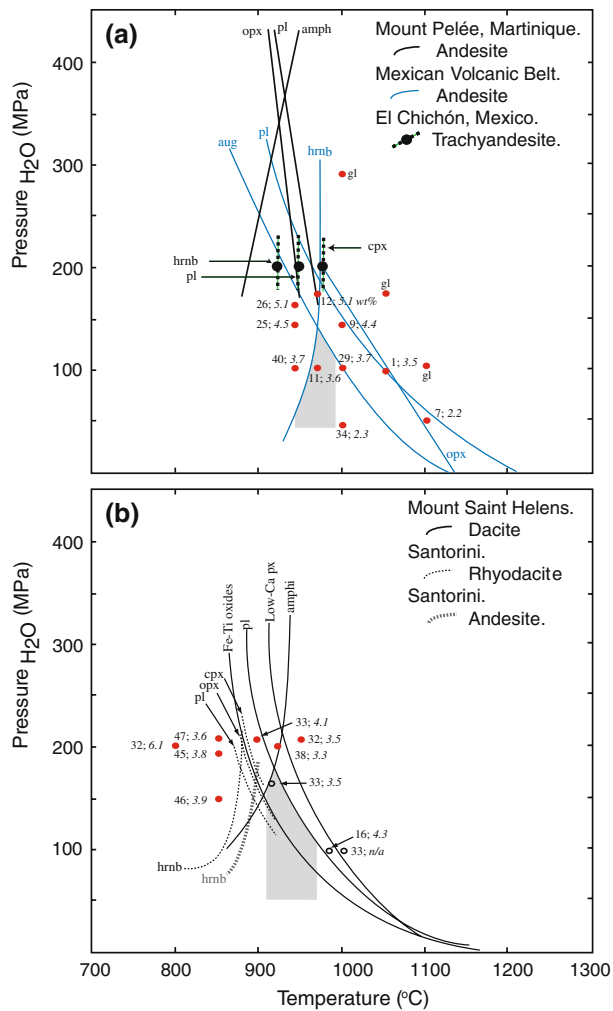


Fig. 11 Experimentally determined pressure-temperature phase diagram. **a** Andesitic compositions from El Chichón (Luhr 1990), the Mexican Volcanic Belt (Moore and Carmichael 1998), and Mt Pelée (Martel et al. 1999). Gray shaded area shows the range of P/T conditions inferred for the 1991 and 6700 trachyandesites based on geothermometry and volatile content estimates. Filled circles and corresponding numbers are experimentally derived crystallinity and H₂O in melt (in *italics*) in weight percent from Moore and Carmichael (1998). Modified from Kratzmann et al. (2009). **b** Compositions from San Pedro (Costa et al. 2004), Santorini (Cottrell et al. 1999), and Mt. St. Helens (Rutherford et al. 1985). Gray shaded area shows the range of P/T conditions inferred for the 3600 trachydacite. Filled circles (Costa et al. 2004) and open circles (Rutherford et al. 1985) and corresponding numbers are experimentally derived crystallinity and H₂O in melt (in *italics*) in weight percent. *amph* amphibole, *aug* augite, *cpx* clinopyroxene, *opx* orthopyroxene, *pl* plagioclase, *gl* glass

Mt St. Helens (16–37%, calculated from Rutherford et al. 1985) experiments encompasses the 3600 values (Table 2). At lower temperatures and higher water contents or higher pressures, hornblende is present in the phenocryst assemblage in the experiments (e.g., Rutherford et al. 1985; Scaillet and Evans 1999; Costa et al. 2004). Overall, the comparisons to experimental work can constrain the

trachydacite pre-eruptive storage conditions to ≤ 200 MPa (Fig. 11b), at approximately 942°C (± 24) and $\log f_{\text{O}_2} -10.68$ (± 0.16), with 2–3 wt% H₂O in the melt.

Discussion

The SVZ is one of the few places along the Andean margin of South America where basaltic end members are included in suites of volcanic rocks from individual centers. It therefore provides an important location to assess the petrogenetic relationships of a potential co-genetic series that span typical calc-alkaline ranges. Hudson volcano, which lies near the tectonic border of the SVZ, may also provide further insights into magmatic processes that occur in association with complex subduction configurations, such as a down-going ocean ridge. Because there is a complete spectrum of magma compositions at Hudson, we hypothesize that the voluminous trachyandesites and trachydacites involved in the highly explosive eruptions during the Holocene are most likely derived from more mafic source magmas by fractional crystallization, coupled with magma mixing. We will use major and trace elements to assess a number of petrogenetic questions including: (1) is there a co-genetic relationship between the explosively erupted magmas (trachyandesite and trachydacite) and mafic lavas at Hudson that can satisfy both major and trace element patterns, and (2) at what depths do important differentiation processes take place beneath the volcano.

We start by characterizing potential parent magmas. Two types of basalt have been defined along the SVZ, with type-1 basalts having lower contents of LILE and HFSE relative to type-2 (López-Escobar et al. 1993). At Hudson volcano an older, Upper Holocene to Late Pleistocene sequence (type-1) with elevated K/Rb, Ba/La, Rb/Cs and lower La/Yb, Rb/Sr and TiO₂ relative to the younger (Late Holocene to Recent) type-2 basalts have been identified by Kilian et al. (1993). The composition of type 2 basalts from both López-Escobar et al. (1993) and Kilian et al. (1993) are very similar, displaying overlapping fields. The most recent basalts erupted at Hudson in 1991 are similar to Pleistocene/Holocene samples analyzed by Gutiérrez et al. (2005) and overlap the type 2 basalts defined by Kilian et al. (1993). Gutiérrez et al. (2005) have also defined the most primitive magmas in the area surrounding Hudson volcano as those from the coeval Río Ibáñez monogenetic cone (15 km to the southeast), whose compositions are similar to samples from the Chile Ridge. The Río Ibáñez compositions overlap both type 1 and type 2 basalts defined by López-Escobar et al. (1993) and Kilian et al. (1993). The Río Ibáñez basalts plot as the most primitive compositions along a potential liquid line of descent defined by the Hudson samples analyzed in this study, and may be genetically related to the Hudson

basalts, making them a possible parental source. However, major element modeling of the Río Ibáñez compositions to generate the 1991 basalts using an anhydrous mineral assemblage (that included plagioclase, clinopyroxene, orthopyroxene, olivine, magnetite, ilmenite, and apatite in varying proportions) has so far proven unsatisfactory. Gutiérrez et al. (2005) have suggested that the Río Ibáñez and more evolved Hudson basalts can be related to one another through fractional crystallization of an anhydrous mineral assemblage coupled with assimilation of upper crustal material. However, the crustal composition used in their model differs from the plutonic rocks of the Patagonian Batholith (e.g., Kilian and Behrmann 2003), which are similar in composition to the millimeter scale silicic inclusions found within the Río Ibáñez samples (e.g., Gutiérrez et al. 2005). The batholiths are the likely assimilant for any magma body rising beneath Hudson volcano.

Given the close temporal (~ 3 days apart), spatial (~ 4 km apart), and possible genetic relationships between the basaltic and trachyandesitic phases of the 1991 eruption (e.g., Kratzmann et al. 2009), the 1991 basalts may be the most likely parental magma type to the more evolved compositions erupted during the 3600 and 6700 events. The underlying assumption is that recharge at Hudson volcano has involved a mafic composition similar to the 1991 basalt and that this composition has not changed significantly during the Holocene.

Origin of the trachyandesite and trachydacite magmas

Major element modeling

Generation of the trachyandesite and trachydacite magmas from a mafic parent similar in composition to the 1991 basalts was modeled by crystal fractionation using the Igpet[®] least squares analysis program (Carr 2005).

The largest Holocene eruption of Hudson volcano produced >4 km³ of trachyandesite magma during the 6700 event. Given the similarities in major elements between the 1991 and 6700 trachyandesites, the formation of the 6700 magma was modeled using the most primitive 1991 basalt composition as the parent. Fractional crystallization of plagioclase ($\sim 28\%$), clinopyroxene ($\sim 25\%$), orthopyroxene ($\sim 2\%$), magnetite ($\sim 12\%$), ilmenite ($\sim 1\%$) and apatite ($\sim 2\%$) yields a strong fit to the average 6700 trachyandesite with a sum of squares of residuals ($\sum r^2$) of 0.026 (Table 9). Variations in the trachyandesite melt compositions (from 63 to 65 wt% SiO₂; Fig. 7c) are likely due to variable amounts of mixing of the trachyandesite with more mafic melts. For example, mixing between the basaltic parent [~ 6 –12 vol.% (49–53 wt% SiO₂)] and the evolved trachyandesite [~ 94 –88 vol.% (64–65 wt% SiO₂)] can reproduce the major element trend of the 6700 glasses with a $\sum r^2$ range of 0.080 to 0.114. This is supported by the occurrence of melt inclusion compositions that are significantly more evolved than the coexisting matrix glass (Fig. 7c) and zonation patterns in plagioclase phenocrysts.

After approximately 3000 years of repose, the next major explosive eruption of Hudson produced ~ 4 km³ of trachydacite magma during the 3600 event. Unlike the 6700 trachyandesite, the trachydacite is very uniform in composition. In addition, there is no significant difference between melt inclusion compositions and the coexisting matrix glasses (Fig. 7d), suggesting little evidence of magma mixing. There are two potential origins for the 3600 trachydacite. Firstly, trachyandesite remaining in a crustal reservoir following the 6700 eruption may have continued to crystallize yielding the trachydacite. Fractionation of plagioclase ($\sim 10\%$), clinopyroxene ($\sim 2\%$), orthopyroxene ($\sim 2\%$), magnetite ($\sim 1\%$), ilmenite ($\sim 2\%$) and apatite ($\sim 1\%$) can yield the trachydacite composition with a $\sum r^2$ of 0.025 (Table 9). Alternatively, the

Table 9 Summary of least squares modeling calculations for the Hudson samples using an anhydrous mineral assemblage

Parent	91-P1-tr.1	91-P1-tr.2	6700.tr.7	91-P1-tr.1	91-P1-tr.2	91-P1-tr.2	RI-128
Daughter	6700.tr.2	6700-ave	3600.tr.1	3600.tr.1	3600.tr.2	3600.tr.2	91-P1.tr.3
SiO ₂ range	49.8–63.1	52.7–64.0	64.9–68.0	49.8–68.0	52.7–68.6	52.7–68.6	49.9–52.7
$\sum r^2$	0.026	0.065	0.025	0.065	0.088	0.020	0.411
Percentage of phase removed							
opx	1.6	0.1	1.4	3.0	2	1.6	
cpx	25.6	18.9	1.9	26.4	19.4	19.0	
pl	28.1	24.1	10.6	37.1	34.4	30.6	pl 33.4
mg	11.8	10.4	1.7	11.6	1.6	11.0	ol 13.0
il	0.7	0.3	0.7	1.9	10.4	1.0	gt 2.1
ap	1.9	1.6	0.3	2.2	2	2.0	
Percentage total	69.7	55.4	16.6	82.2	69.8	65.2	Percentage total 48.5

$\sum r^2$ sum of squares of residuals, *P1* phase 1, *tr* translucent glass, *ave* average composition, *RI* Río Ibáñez, *opx* orthopyroxene, *cpx* clinopyroxene, *pl* plagioclase, *mg* magnetite, *il* ilmenite, *ap* apatite, *ol* olive, *gt* garnet

trachydacite may have been derived from more extensive crystallization of a new influx of basaltic parental melt. Fractional crystallization of plagioclase (~34%), clinopyroxene (~20%), orthopyroxene (~2%), magnetite (~2%), ilmenite (~10%) and apatite (~2%) from a basaltic parental melt can also yield the 3600 trachydacite composition with a $\sum r^2$ of 0.065 (Table 9). Both solutions give excellent fits in terms of major elements and it is not possible to discriminate between the two possible origins based only on major element models.

The most recent eruption of Hudson in 1991 was the first example of the simultaneous discharge of both basaltic and trachyandesite magmas. It is possible, however, that the 3600 and 6700 events erupted in a similar fashion but the products may have had a limited dispersal and have subsequently been eroded or covered by more recent deposits. Our 2005 field program was not able to gain access to proximal outcrops around Hudson volcano and thus we relied on samples of the more widespread 3600 and 6700 fallout deposits. Combined petrologic and geochemical data indicates that the 1991 basalt and trachyandesite magmas can be related through both fractional crystallization and magma mixing (Kratzmann et al. 2009). The crystallizing assemblage consists of plagioclase, clinopyroxene, orthopyroxene, magnetite and apatite yielded $\sum r^2$ values from 0.06 to 0.09.

The evolution of the major elements could be successfully reproduced using multiple combinations of minerals, precipitating in varying proportions, from either an anhydrous or a hydrous mineral assemblage (i.e., one that includes amphibole). Discrimination between anhydrous and hydrous phase assemblage becomes more apparent when trace element trends are considered (see following section).

Trace element modeling

Based on the results from the major element modeling, select trace element abundances in the natural samples (e.g., Rb, Ba, Th, Nb, Ta, La, Ce, Nd, Sm, Zr, Hf, Eu, Y, Tm, Yb, Lu) have been used to verify and refine the geochemical modeling. Calculations using the Rayleigh fractionation equation $C_1 = C_0 F^{(D-1)}$ were conducted to test the predictions of the major element modeling, where C_1 is the concentration of an element in the liquid, C_0 the concentration of an element in the original liquid, F is the fraction of liquid remaining, and D is the bulk partition coefficient. The bulk partition coefficients used in the calculations are given in Supplementary Table S2.

Anhydrous mineral assemblage

Calculated fractionation curves are shown for Y, Hf, Zr, Ce, La, and Dy/Yb for the removal of an anhydrous

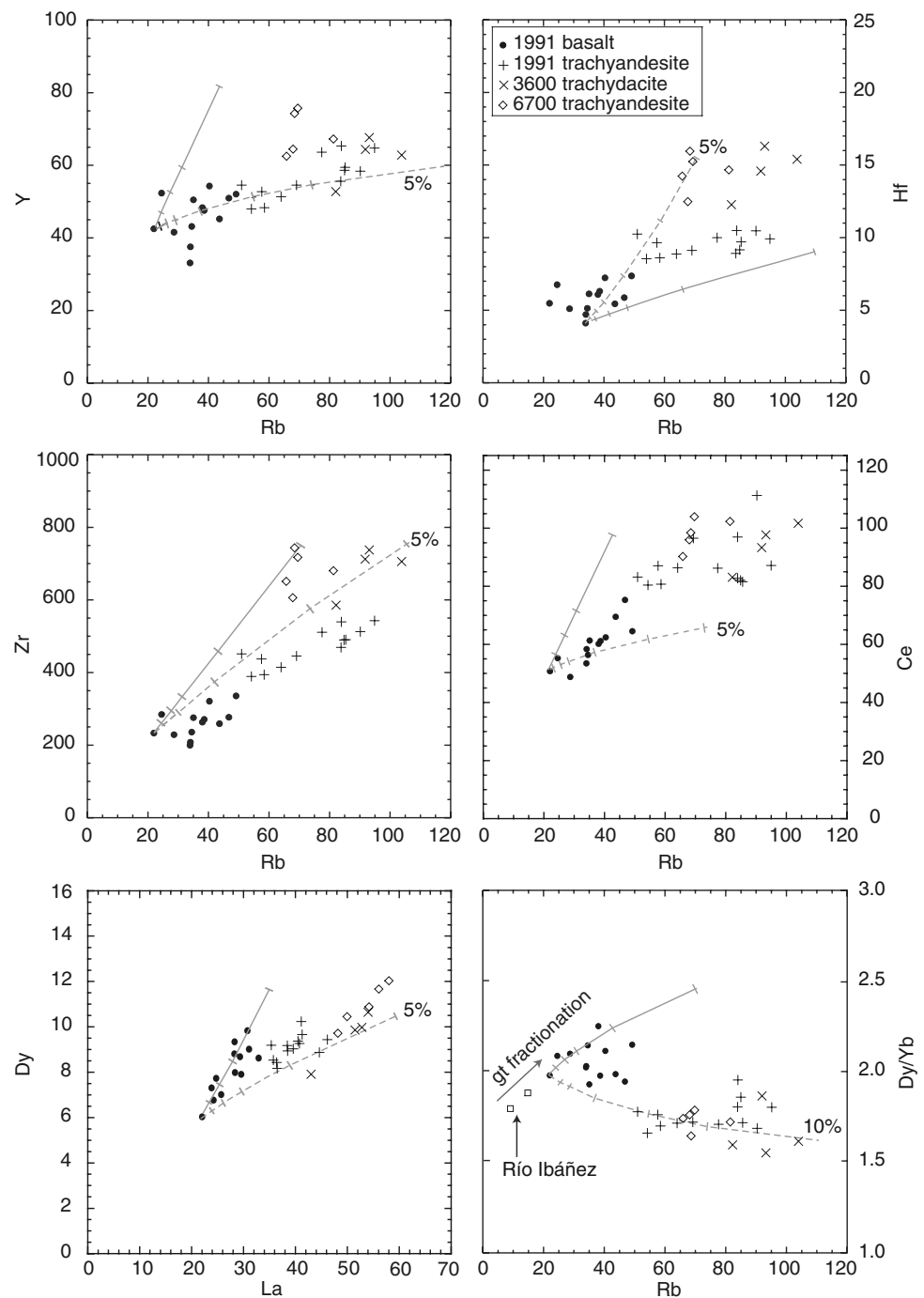
mineral assemblage that includes clinopyroxene, orthopyroxene, plagioclase, magnetite, ilmenite, and apatite in varying proportions (Fig. 12). The results indicate that crystal fractionation involving an anhydrous mineral assemblage can successfully reproduce the concentrations of Hf, Zr, and Th in the evolved compositions. Fractionation via an anhydrous mineral assemblage can also account for the variation of Ce, Dy/Yb, and La/Yb within the 1991 basaltic andesite. However, on plots of Ce versus Rb and Dy/Yb versus Rb (Fig. 12) it can be seen that the calculated curve does not trend towards the higher concentrations of the evolved glasses. While the calculated fractionation curve for La/Yb can reproduce the trend in the data from the 1991 basaltic andesite to the 1991 trachyandesite (not shown), the anhydrous assemblage cannot replicate the elevated concentrations of the 6700 and 3600 samples. In addition, the calculated fractionation curve for Y diverges from the glass trend when using an anhydrous mineral assemblage (Fig. 12).

Hydrous mineral assemblage

Despite the excellent fits to the major and select trace element data (e.g., Hf, Zr, and Th) of the trachyandesites and trachydacites, there are certain trace elements (e.g., La, Dy, Y and Ce) whose trends are not well explained by fractionation of the observed anhydrous mineral phases present in the Hudson magmas (Fig. 12). The elevated concentrations of these trace elements within the more evolved trachyandesitic and trachydacitic compositions can be successfully reproduced through the addition of between 2 and 10% amphibole to the fractionating mineral assemblage. This is clearly visible in the Y, Ce, and Dy/Yb versus Rb plots (Fig. 12) where the calculated fractionation curves shift dramatically in the direction of the more evolved compositions.

Davidson et al. (2007) have recently suggested that the ratios of La/Yb and Dy/Yb can be effectively used to infer the signature of pressure-dependent phase assemblages, such as garnet (deep) or amphibole (moderate/deep) during crystallization of calc-alkaline arc suites, due to characteristic differences in the mineral/melt partition coefficients. In particular, a trend of decreasing Dy/Yb ratio with increasing degree of differentiation indicates amphibole fractionation within an arc suite. On such a plot, the basalt to trachydacite Hudson suite exhibits a decrease in Dy/Yb with increasing SiO₂ that is similar in magnitude to other arc suites such as the Aleutian Islands and volcanic centers from Java (Fig. 10). The combined trends of Dy/Yb and La/Yb versus SiO₂ for the Hudson compositions are therefore suggestive of amphibole crystallization without any contribution from garnet. Using the 1991 basalt as a starting point, the modeling of certain

Fig. 12 Representative trace elements versus degree of differentiation. Model fractionation curves are for an anhydrous (*solid gray line*), and a hydrous (*dashed grey line*) mineral assemblages. Percentage values shown indicate the amount of amphibole added to the fractionating assemblage. Differentiation of the Río Ibáñez samples involving garnet would increase the Dy/Yb ratio of the derivative melts (*gray arrow*, Dy/Yb vs. Rb plot)



trace elements, such as La, Dy, Y, and Ce is improved by the addition of amphibole to the crystallizing assemblage of the Hudson suite. Addition of 2–10% amphibole over the entire range of fractionation can generate elevated trace element concentrations similar to the 1991 trachyandesite, 3600 trachydacite, and 6700 trachyandesite (Fig. 12).

An exception to the generally decreasing Dy/Yb ratio in the Hudson suite are the compositions of the nearby Río

Ibáñez basalts. Compared to the 1991 basalts, the more primitive Río Ibáñez samples have lower values of Dy/Yb. Geochemical modeling of the Río Ibáñez basalt to Hudson 1991 basaltic andesite (this study) with garnet as a fractionating phase results in elevated La/Yb and Dy/Yb ratios (Figs. 10, 12). If the Río Ibáñez compositions are parental to 1991-type basalts this may indicate deep crustal fractionation involving garnet (Fig. 12; e.g., Davidson et al. 2007).

Deep versus shallow crustal differentiation of trachyandesite and trachydacite

Both deep (lower crust) and shallow (upper crust) level differentiation of magmas have been inferred for centers along the Andean margin, including Hudson volcano. For example, differentiation of mantle-derived basaltic magmas at deep crustal levels (where garnet is stable) has been inferred at Volcán Ollagüe [21°S; Andean Central Volcanic Zone (Feeley and Davidson 1994)]. Also, lower crustal differentiation (~800 MPa) of basalts to basaltic andesites has been proposed at Planchon volcano in the transitional SVZ (34.5–37°S; e.g., Tormey et al. 1991), and for the type-2 basalts defined by López-Escobar et al. (1993). In contrast, there is evidence of shallow level (<300 MPa) differentiation of basalt to more evolved compositions (i.e., andesite to rhyolite) along the entire length of the SVZ (e.g., Tormey et al. 1991; López-Escobar et al. 1993; Feeley and Davidson 1994), including Hudson volcano (e.g., Gutiérrez et al. 2005).

No evidence is found for garnet fractionation in the Hudson suite. For example, there is no systematic variation in Ce/Yb versus Yb, whereas if garnet were a fractionating phase a strongly decreasing trend would be expected (e.g., Feeley and Davidson 1994). Similarly, there is no HREE depletion in the REE patterns of the Hudson samples (Fig. 9), as would be expected if garnet was part of the crystallizing assemblage. Tormey et al. (1991) proposed deep crustal differentiation (e.g., ~800 MPa) of basalts and basaltic andesites at Planchon volcano (transitional SVZ) based on the trend of increasing Al₂O₃ with decreasing MgO. The depth of differentiation was further constrained to between ~400 and 800 MPa by Tormey et al. (1995) based on the mafic samples plotting between the experimentally determined 200 and 800 MPa cotectics (e.g., Sisson and Grove 1993; Gust and Perfit 1987, respectively), when plotted on a olivine–clinopyroxene–quartz ternary diagram (e.g., Grove et al. 1982). The mafic samples from Hudson volcano also exhibit an Al₂O₃–MgO trend similar to that of Planchon volcano, but plot close to the experimentally determined 200 MPa cotectic (e.g., Sisson and Grove 1993) when plotted on the ol–cpx–qtz ternary diagram.

The fractionation of amphibole places some constraints on the depth at which differentiation may have occurred. Experimental determinations of the amphibole stability curves in basaltic andesite compositions (e.g., Moore and Carmichael 1998) suggest an inflection at about 200 MPa where the slope decreases towards lower pressure (Fig. 11). The change in orientation of this boundary is sub-parallel to a simple decompression path and crossing this stability curve would result in amphibole instability (Davidson et al. 2007). Thus, amphibole fractionation is

likely to have occurred at depths of greater than 6 km. The lack of a clear garnet signal in the trace element data suggests that differentiation does not occur at deep levels, but takes place somewhere between the depths of garnet stability and amphibole stability. The initial staging point for the differentiation of the parental mafic magmas may be the lower crustal ‘hot zone’ model (~20 km) of Annen et al. (2006), with the amphibole-rich cumulates contributing to the amphibolite facies inferred to be at ~24 km (e.g., Rudnick and Fountain 1995). Together these may place some constraint on the lower limit of depth of differentiation (i.e., ~700–800 MPa).

Within the trace element data for the Hudson suite, there is no evidence for garnet as a residual phase but the data do suggest that amphibole may have played an important role in the genesis of the Holocene magmatic suite (Figs. 11, 12). The paradox of this model is that amphibole is not found as a phenocryst phase in any of the Hudson volcanics. Davidson et al. (2007) cite this relationship for many arc suites, suggesting that amphibole crystallization occurs at deeper levels in the crust with the amphibole phenocrysts left behind as a restite before the magma ascends and passes outside of the amphibole stability field at lower pressures (<6 km). This may have been the case for the Hudson magmas based on trace element trends (i.e., La/Yb and Dy/Yb versus SiO₂). The trend of decreasing Dy/Yb with increasing degree of differentiation in the Hudson suite cannot be explained by shallow fractionation without amphibole. Therefore, we suggest that modification of the Hudson basaltic magmas occurs at upper-mid crustal below 6 km (and potentially to lower crustal levels ~20–24 km). The crystallizing assemblage includes amphibole, which is physically separated from the magma in order to generate the Dy/Yb trend. Subsequent derivative magmas rise to shallow levels prior to eruption and undergo degassing, crystallization, and melt inclusion entrapment. Additional evolution of the liquids may occur as a result of these combined processes until eruptions tap into the shallow reservoirs.

Model for magma differentiation

Major and trace element modeling suggests that the voluminous trachyandesite and trachydacite magmas erupted explosively at Hudson volcano during the Holocene can be derived from a basaltic parent with modification by mixing during periodic recharge events. Although the modeling suggests fractional crystallization alone can successfully produce the range occupied by the more evolved plinian-style eruptions, petrologic textures and melt inclusion data suggest magma mixing also plays an important role in the compositional diversity of evolved Hudson magmas and therefore, must be included in any model[s] of magma

formation. Here we present a model (in chronological eruption order) for magma genesis at Hudson volcano that includes crystal fractionation, recharge, and mixing to produce the more evolved compositions.

The most primitive basaltic magmas are generated by partial melting of a fluid-modified MORB-like source (Gutiérrez et al. 2005). These melts, represented to some extent by compositions erupted from monogenetic cones surrounding Hudson (e.g., Río Ibáñez and Murta), ascend, fractionate and assimilate crustal material (Gutiérrez et al. 2005). Fractionation may have involved garnet at deep levels (>45 km), as indicated by the higher Dy/Yb ratio of the Hudson basalts relative to the Río Ibáñez samples (Figs. 10, 13). These processes result in the formation of more evolved, hydrous basalts and basaltic andesites (50–54 wt% SiO₂) similar to those erupted in 1991. The trace element modeling suggests a role for amphibole in the further differentiation of the Hudson basalts and basaltic andesites.

The generation of the voluminous trachyandesite erupted during the 6700 yrs BP event can be effectively

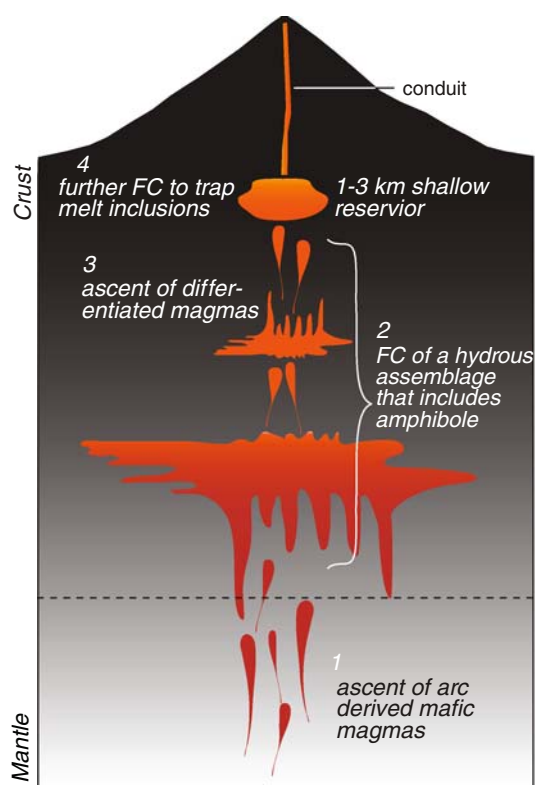


Fig. 13 Model for the Holocene eruptions at Hudson volcano. 1 Slab dewatering and primary melt generation. 2 Mantle-derived melts ponding in the mid to lower crust (~ 6 –24 km) where crystal fractionation involving a hydrous mineral assemblage that includes amphibole generates the more evolved compositions. 3 Derivative melts, now carrying the geochemical signature of amphibole, ascend and stall in the shallow crust where they undergo low-pressure fractionation via an anhydrous mineral assemblage prior to eruption

modeled by fractional crystallization of the evolved basalts. A genetic relationship between the 1991-type basalts and the trachyandesite is supported by the similarity in strontium isotope ratios (López-Escobar et al. 1993; Naranjo and Stern 1998; Stern 2008). However, the distinctive trend of decreasing Dy/Yb ratio with increasing differentiation in the suite strongly suggests a role for amphibole fractionation (Fig. 10), even though this phase is not present in the erupted magmas. The inflection in the amphibole stability curve (~ 200 MPa; e.g., Moore and Carmichael 1998) places some constraints on the depth at which differentiation may have occurred (i.e., <6 km). Amphibole fractionation may occur at any point below 6 km and extend to 20–24 km depth [e.g., ‘hot zone’ model (Annen et al. 2006); amphibolite facies (Rudnick and Fountain 1995)], but not to depths where garnet is stable (>45 km). Therefore, we suggest that the inferred amphibole fractionation takes place at depths below 6 km and potentially at depths to ~ 20 –24 km. Modeled solutions based on the fractionation of plagioclase, pyroxene, amphibole and Fe–Ti oxides yields excellent fits to both major and trace element patterns. The amphibole phenocrysts may have been physically separated and left behind as restite in the lower crust before the ascending melt, which now carries the signature of cryptic amphibole fractionation (e.g., Davidson et al. 2007), passed out of the amphibole stability field. We suggest that just prior to the 6700 eruption, trachyandesite magma rose to relatively shallow levels (<2 km) where a reduction of pressure resulted in amphibole becoming unstable and being replaced by an anhydrous assemblage of plagioclase, pyroxenes and Fe–Ti oxides. Pressure decrease may have also triggered additional crystallization, accompanied by melt inclusion entrapment (Blundy et al. 2006). Volatile contents in the melt inclusions thus reflect the rather shallow storage level just prior to eruption. Another consequence of degassing is a potential increase in temperature associated with the latent heat of crystallization, estimated at $\sim 3^\circ\text{C}$ per percent crystallization (e.g., Blundy et al. 2006). Based on the maximum crystallinity of the Hudson samples (Table 2), this would produce a temperature increase on the order of $\sim 80^\circ\text{C}$. Given the speed at which Fe–Ti oxides can re-equilibrate (e.g., Venezky and Rutherford 1999) this may explain why the Fe–Ti oxide temperatures of the 6700 trachyandesite are higher than the upper limits of amphibole stability (e.g., Rutherford et al. 1985) at about 900°C (at <200 MPa; Fig. 11b). The pre-eruptive storage of the 6700 trachyandesite occurred at depths between 1.0 and 1.4 km at approximately $972 \pm 25^\circ\text{C}$ and $\log f\text{O}_2 -10.24 \pm 0.2$, under water-saturated conditions (based on estimates of the volatile content in melt inclusions and mineral geothermometry).

An important observation about the 6700 trachyandesite is the range of melt compositions (matrix glasses) and their relationship to melt inclusions (Fig. 7c). The occurrence of melt inclusions that are more evolved than the coexisting matrix glasses suggests magma mixing. It is possible to rule out host crystallization as the cause for the evolved character of the melt inclusions based on simple trends of major elements such as FeO and K₂O. Thus it is likely that mixing of the trachyandesite with more mafic melts can explain the compositional diversity of the melts and their relationship to the melt inclusions. Modeling of the matrix glass compositional spread by magma mixing of trachyandesite with evolved basalts yields very good fits to the data. It is difficult, however, to specify at what point mixing occurred. It may have taken place at deeper levels during amphibole fractionation (~20–24 km) or just prior to eruption when the trachyandesite had ascended to shallow levels (<2 km).

Derivation of the 3600 trachydacite is also attributed ultimately to fractional crystallization involving amphibole because of the trend of decreasing Dy/Yb in this most evolved endmember (Fig. 10b). This composition can be attained by up to 70% fractionation of plagioclase, pyroxene, amphibole, Fe–Ti oxides and apatite from a basaltic parent or alternatively, by ~25% fractionation of residual trachyandesite produced prior to the 6700 event. The similarity of strontium isotope ratios of the 3600 trachydacite [~ 0.70445 (Naranjo and Stern 1998)] to the 6700 trachydacite [~ 0.70450 (Stern 2008)] supports a genetic link for the latter process. We also suggest that the 3600 trachydacite rose to relatively shallow levels (<2 km) prior to eruption and moved outside the stability field of amphibole resulting in the presence of only an anhydrous mineral assemblage (plagioclase, pyroxene, Fe–Ti oxides) at the time of eruption. Degassing-induced melt inclusion entrapment recorded the shallow level signature of the storage region. The pre-eruptive storage of the 3600 trachydacite occurred at depths between 1.1 and 2.0 km at approximately 942°C (± 24) and $\log fO_2 -10.68$ (± 0.2) (assuming water-saturated conditions). Unlike the 6700 trachyandesite, the 3600 trachydacite shows a high degree of similarity between melt inclusion compositions and coexisting matrix glasses. This suggests that there was not significant magma mixing in the main part of the 3600 storage region prior to eruption.

The most recent 1991 eruption was unique in that magmas of contrasting composition (basalt and trachyandesite) were erupted only days apart, from different vents within the summit caldera. Kratzmann et al. (2009) proposed that the trachyandesite from the paroxysmal phase of the eruption could be related to the early erupted basalts through fractional crystallization and magma mixing. Major element modeling produced excellent fits based on

the anhydrous assemblage of plagioclase, olivine, pyroxene, Fe–Ti oxides, and apatite. However, addition of amphibole to the crystallizing assemblage better explains the decrease in Dy/Yb ratio that is present in the 1991 suite. This also suggests that the latest eruptive products carry the geochemical signature of cryptic amphibole crystallization. As with the 6700 and 3600 events, the lack of amphibole in the eruptive products is attributed to shallow pre-eruption storage outside the amphibole stability field. Based on estimates of volatile content in melt inclusions and mineral geothermometry, and assuming water-saturated conditions, pre-eruptive storage of the 1991 trachyandesite occurred at pressures between 0.2 and 2.7 km depth, at approximately 972°C (± 26) and $\log fO_2 -10.33$ (± 0.2).

Magma mixing, involving basalt and trachyandesite, is also required to explain the systematic trend towards more mafic melt compositions in the latter stages of the paroxysmal phase (Kratzmann et al. 2009). Withdrawal of magma from deeper levels as the eruption progressed tapped into areas where mafic magma had mixed with and hybridized the dominant trachyandesite magma. The intrusion of more mafic magma into the trachyandesite storage region may have contributed to triggering of the eruption sequence.

Conclusions

The Holocene explosive eruptions of Hudson volcano in southern Chile have consistently discharged magmas of similar composition (trachyandesite and trachydacite), comparable anhydrous phenocryst assemblages (plagioclase, pyroxene, Fe–Ti oxides, \pm olivine), and pre-eruptive temperatures (943–972°C) and oxygen fugacities. Geochemical modeling suggests that the evolved magmas can be derived from a basaltic parent primarily via fractional crystallization. Pre-eruptive storage conditions for the Holocene magmas have been estimated based on the volatile contents in melt inclusions, mineral geothermometry, and comparisons to analogous experimental work. The pressures obtained from the analysis of melt inclusions all suggest shallow levels of entrapment (<100 MPa; assuming water saturation). Storage of the 6700 years BP trachyandesite occurred at depths between 1.0 and 1.4 km at approximately 972 \pm 25°C and $\log fO_2 -10.24 \pm 0.2$, with up to ~2 wt% H₂O in the melt. The 3600 years BP trachydacite storage occurred at similar depths between 1.1 and 2.0 km but at a slightly lower temperature of 942°C (± 24) and $\log fO_2 -10.68$ (± 0.2), and approximately 2.5 wt% H₂O. The most recent pre-eruptive storage of the trachyandesite, erupted in 1991, occurred at depths ranging from 0.2 to 2.7 km, a temperature of 972°C (± 26), $\log fO_2 -10.33 \pm 0.2$, and 1–3 wt% H₂O in the melt. However, an

important role for amphibole in the differentiation of the Hudson magmas is suggested in the trace element data (specifically La/Yb and Dy/Yb ratio trends). An upper limit for this differentiation is suggested by the sub-parallel nature of the amphibole stability curve, and is likely to have occurred at depths of greater than six kilometers. A potential lower depth limit for the role of amphibole is suggested by the depth of contact between the upper and lower crust [~ 20 km (Annen et al. 2006)], and the estimated depth to an amphibolite facies [~ 24 km (Rudnick and Fountain 1995)].

During the Holocene activity at Hudson volcano, mantle-derived magmas stalled between upper-mid and lower crustal levels (~ 6 – 24 km) and differentiated to more evolved compositions by crystal fractionation involving a hydrous mineral assemblage (Fig. 13). This resulted in the formation of slightly more evolved basaltic magma similar in composition to the first phase of the 1991 eruption. Continued fractional crystallization at depth generated the trachyandesitic and trachydacitic compositions of the 6700 years BP, 3600 years BP, and 1991 eruptions. Amphibole phenocrysts may have been retained in this differentiation zone as a relict. During the 6700 years BP and 3600 years BP events, the evolved magmas ascended from mid to lower crustal depths and temporarily stalled in the shallow crust. At this point they crossed out of the amphibole stability field and further crystallization involved an anhydrous mineral assemblage. This shallow level fractionation is suggested by the pressures of entrapment obtained from the melt inclusion data. Furthermore, this decompression crystallization may have resulted in the heating of the magma body (e.g., Blundy et al. 2006) which shifted the temperature outside the thermal stability field of amphibole (e.g., Rutherford et al. 1985). The decrease in pressure, increase in temperature, and resultant crossing of the amphibole stability curve may explain the lack of phenocrystic amphibole in the Hudson samples. The 1991 trachyandesite followed a similar evolution, ascent, and crystallization path as the previous eruptions. However, coincident to its shallow emplacement, some of the parent basaltic magma also ascended into the shallow crust prior to erupting. It mixed with and hybridized the stalled trachyandesite before erupting in the north-western corner of the caldera. The 1991 basalt was a potential trigger for the 1991 trachyandesitic eruption (e.g., Naranjo et al. 1993; Kratzmann et al. 2009) and basaltic intrusions beneath Hudson may have played a role in initiating the other large explosive eruptions.

Acknowledgments The authors thank Alejandro Bande for assistance during fieldwork in 2005. Many thanks go to J. D. Devine, C. W. Mandeville, K. A. Kelley, N. A. Hamidzada and M. Lytle for

assistance and expertise during data collection. The manuscript benefited from reviews by K. A. Kelley, O. D. Hermes, J. P. Davidson and an anonymous reviewer. This research was supported by NSF grant EAR-0337023 to Carey and Scasso. JAN acknowledges Fondcyt Project 1960186 and Sernageomin's Volcanic Hazard Programme.

References

- Andersen DJ, Lindsley DH (1988) Internally consistent solution models for Fe–Mg–Mn–Ti oxides: Fe–Ti oxides. *Am Mineral* 73(7–8):714–726
- Andersen DJ, Lindsley DH, Davidson PM (1993) QUILF: a pascal program to assess equilibria among Fe–Mg–Mn–Ti oxides, pyroxenes, olivine, and quartz. *Comput Geosci* 19:1333–1350
- Anderson AT (1973) The before-eruption water content of some high-alumina magmas. *Bull Volcanol* 37(4):530–552
- Annen C, Sparks RSJ (2002) Effects of repetitive emplacement of basaltic intrusions on thermal evolution and melt generation in the crust. *Earth Planet Sci Lett* 203(3–4):937–955
- Annen C, Blundy JD, Sparks RSJ (2006) The genesis of intermediate and silicic magmas in deep crustal hot zones. *J Petrol* 47(3):505–539
- Bacon CR, Hirschmann MM (1988) Mg/Mn partitioning as a test for equilibrium between coexisting Fe–Ti oxides. *Am Mineral* 73:57–61
- Bebout GE (1991) Field-based evidence for devolatilization in subduction zones: implications for Arc magmatism. *Science* 251(4992):413–416
- Bitschene PR, Fernández MI (1995) Volcanology and petrology of fallout ashes from the August 1991 eruption of the Hudson Volcano (Patagonian Andes). In: Bitschene P, Medina J (eds) *The August 1991 eruption of the Hudson Volcano (Patagonian Andes); a thousand days after*. Cuvillier, Gottingen, pp 27–54
- Bitschene PR, Fernández MI, Arias N, Arizmendi A, Griznik M, Nillni A (1993) Volcanology and environmental impact of the August 1991 eruption of the Hudson volcano (Patagonian Andes, Chile). *Zbl Geol Palaont Teil IH* 1(2):165–177
- Blundy J, Cashman K, Humphreys M (2006) Magma heating by decompression-driven crystallization beneath andesite volcanoes. *Nature* 443(7107):76–80
- Carey S, Scasso RA, Kratzmann D, Naranjo JA, Bande A (2005) Stratigraphy and Melt Compositions of the 3.6 and 6.7 ka Plinian Eruptions of Hudson Volcano, Chile. *AGU Fall Meeting 2005*. Posters V41B-1443 San Francisco
- Carr M (2005) Iqpet Software. CD-ROM.
- Costa F, Scaillet B, Pichavant M (2004) Petrological and experimental constraints on the pre-eruption conditions of Holocene Dacite from Volcán San Pedro (36°S, Chilean Andes) and the importance of sulphur in silicic subduction-related magmas. *J Petrol* 45(4):855–881
- Cottrell E, Gardner JE, Rutherford MJ (1999) Petrologic and experimental evidence for the movement and heating of the pre-eruptive Minoan rhyodacite (Santorini, Greece). *Contrib Mineral Petrol* 135(4):315–331
- Davidson J, Turner S, Handley H, Macpherson C, Dosseto A (2007) Amphibole “sponge” in arc crust? *Geology* 35(9):787–790
- Devine JD, Gardner JE, Brack HP, Layne GD, Rutherford MJ (1995) Comparison of microanalytical methods for estimating H₂O contents of silicic volcanic glasses. *Am Mineral* 80:319–328
- Dixon JE, Stolper EM (1995) An experimental study of water and carbon dioxide solubilities in mid-ocean ridge basaltic liquids. Part II: applications to degassing. *J Petrol* 36(6):1633–1646

- Feeley TC, Davidson JP (1994) Petrology of calc-alkaline lavas at Volcán Ollagüe and the origin of compositional diversity at central Andean stratovolcanoes. *J Petrol* 35(5):1295–1340
- Forsythe RD, Nelson EP (1985) Geological manifestations of ridge collision: evidence from the Golfo de Penas-Taitao basin, southern Chile. *Tectonics* 4:477–495
- Gill JB (1981) *Orogenic andesites and plate tectonics*. Springer, New York, p 390
- Glazner AF (1994) Foundering of mafic plutons and density stratification of continental crust. *Geology* 22:435–438
- Grove TL, Baker MB (1984) Phase equilibrium controls on the tholeiitic versus calc-alkaline differentiation trends. *J Geophys Res* 89(B5):3253–3274
- Grove TL, Kinzler RJ (1986) Petrogenesis of andesites. *Ann Rev Earth Planet Sci* 14:417–454
- Grove TL, Gerlach DC, Sando TW (1982) Origin of calc-alkaline series lavas at Medicine Lake volcano by fractionation, assimilation and mixing. *Contrib Mineral Petrol* 80:160–182
- Gust DA, Perfit MR (1987) Phase relations on a high-Mg basalt from the Aleutian island arc: implications for primary island arc basalts and high-Al basalts. *Contrib Mineral Petrol* 97(1):7–18
- Gutiérrez F, Gioncada A, Gonzalez-Ferran O, Lahsen A, Mazzuoli R (2005) The Hudson Volcano and surrounding monogenetic centres (Chilean Patagonia): An example of volcanism associated with ridge-trench collision environment. *J Volcanol Geoth Res* 145:207–233
- Hammer JE, Rutherford MJ (2002) An experimental study of the kinematics of decompression-induced crystallization in silicic melt. *J Geophys Res* 107(B1):1–24
- Hawkesworth CJ, Gallagher K, Hergot JM, McDermott F (1993) Mantle and slab contributions in arc magmas. *Ann Rev Earth Planet Sci* 21:175–204
- Ippach P (2001) Untersuchung der klimarelevanten Spurengase der Eruption des Cerro Hudson (Süd-Chile) im August 1991. Ph.D. Thesis, Christian Albrechts Universität zu Keil, 159 pp
- Irvine TN, Baragaar WRA (1971) A guide to the chemical classification of the common volcanic rocks. *Can J Earth Sci* 8(5):523–548
- Kelley KA, Plank T, Ludden J, Staudigel H (2003) Composition of altered oceanic crust at ODP Sites 801 and 1149. *Geochem Geophys Geosyst* 4(6):8910. doi:10.1029/2002GC000435
- Kilian R, Behrmann JH (2003) Geochemical constraints on the sources of Southern Chile Trench sediments and their recycling in arc magmas of the Southern Andes. *J Geol Soc* 160:57–70
- Kilian R, Ippach P, López-Escobar L (1993) Geology, geochemistry and recent activity of the Hudson Volcano, Southern Chile. In: Second ISAG. Chile deriva continental geoquímica, Deriva Continental, volcanicas, MORB cretácica, terciaria Oxford
- Kratzmann D, Carey SN, Scasso RA, Naranjo JA (2009) Compositional variations and magma mixing in the 1991 eruptions of Hudson volcano, Chile. *Bull Volcanol* 71:419–439. doi:10.1007/s00445-008-0243-x
- Le Bas MJ, Le Maitre RW, Streckeis A, Zanettin B (1986) A chemical classification of volcanic rocks based on the total alkali silica diagram. *J Petrol* 27:745–750
- Le Bas MJ, Le Maitre RW, Wooley AR (1992) The construction of the total alkali-silica chemical classification of volcanic rocks. *Mineral Petrol* 46(1):1–22
- López-Escobar L, Kilian R, Kempton P, Tagiri M (1993) Petrography and geochemistry of quaternary rocks from the Southern Volcanic zone of the Andes between 41°30' and 46°00'S, Chile. *Rev Geol Chile* 20(1):33–55
- Luhr JF (1990) Experimental phase relations of water- and sulfur-saturated arc magmas and the 1982 eruptions of El Chichón Volcano. *J Petrol* 31(5):1071–1114
- Macpherson CG, Dreher ST, Thirlwall MF (2006) Adakites without slab melting: high pressure differentiation of island arc magma, Mindanao, the Philippines. *Earth Planet Sci Lett* 243(3–4):581–593
- Mandeville CW, Webster JD, Rutherford MJ, Taylor BE, Timbal A, Faure K (2002) Determination of molar absorptivities for infrared absorption bands of H₂O in andesitic glasses. *Am Mineral* 87:813–821
- Martel C, Pichavant M, Holtz F, Scaillet B, Bourdier J-L, Traineau H (1999) Effects of *f*O₂ and H₂O on andesite phase relations between 2 and 4 kbar. *J Geophys Res* 104(B12):29,453–29,470
- Moore G, Carmichael ISE (1998) The hydrous phase equilibria (to 3 kbar) of an andesite and basaltic andesite from western Mexico: constraints on water content and conditions of phenocryst growth. *Contrib Mineral Petrol* 130:304–319
- Moore G, Vennemann T, Carmichael ISE (1998) An empirical model for the solubility of H₂O in magmas to 3 kilobars. *Am Mineral* 83:36–42
- Naranjo JA, Stern CR (1998) Holocene explosive activity of Hudson Volcano, southern Andes. *Bull Volcanol* 59:291–306
- Naranjo JA, Moreno H, Banks N (1993) La erupción del Volcán Hudson en 1991 (46°S), Región XI, Aisén. *Chile Boletín* 44:1–50
- Orihashi Y, Naranjo JA, Motoki A, Sumino H, Hirata D, Anma R, Nagao K (2004) Quaternary volcanic activity of Hudson and Lautaro volcanoes, Chilean Patagonia: New constraints from K-Ar ages. *Rev Geol Chile* 31(2):207–224
- Putirka KD, Perfit M, Ryerson FJ, Jackson MG (2007) Ambient and excess mantle temperatures, olivine thermometry, and active vs. passive upwelling. *Chem Geol* 241:177–206
- Roeder PL, Emslie RF (1970) Olivine-liquid equilibrium. *Contrib Mineral Petrol* 29:275–289
- Rudnick RL, Fountain DM (1995) Nature and composition of the continental crust: a lower crustal perspective. *Rev Geophys* 33:267–309
- Rutherford MJ, Sigurdsson H, Carey S, Davis A (1985) The May 18th, 1980, eruption of Mount St. Helens I. Melt composition and experimental phase equilibria. *J Geophys Res* 90(B4):2929–2947
- Scaillet B, Evans BW (1999) The 15 June 1991 eruption of Mount Pinatubo. I. Phase equilibria and pre-eruption P-T-*f*O₂-*f*H₂O conditions of the Dacite Magma. *J Petrol* 40(3):381–411
- Scasso RA, Carey S (2005) Morphology and formation of glassy volcanic ash from the August 12–15, 1991 eruption of Hudson Volcano, Chile. *Lat Am J Sediment Basin Anal* 12(1):3–21
- Scasso RA, Corbella H, Tiberi P (1994) Sedimentological analysis of the tephra from the 12–15 August 1991 eruption of Hudson volcano. *Bull Volcanol* 56:121–132
- Sisson TW, Grove TL (1993) Experimental investigations of the role of H₂O in calc-alkaline differentiation and subduction zone magmatism. *Contrib Mineral Petrol* 113:143–166
- Stern CR (1991) Mid-Holocene tephra on Tierra del Fuego (54°S) derived from the Hudson Volcano (46°S): Evidence for a large explosive eruption. *Rev Geol Chile* 18(2):139–146
- Stern CR (2004) Active Andean volcanism: its geologic and tectonic setting. *Rev Geol Chile* 31(2):161–206
- Stern CR (2008) Holocene tephrochronology record of large explosive eruptions in the southernmost Patagonian Andes. *Bull Volcanol* 70:435–454. doi:10.1007/s00445-007-0148-z
- Stern CR, Futa K, Muehlenbachs K (1984) Isotope and trace element data for orogenic andesites from the austral andes. In: Harmon RS, Barreiro BA (eds) *Andean magmatism: chemical and isotopic constraints*. Shiva Geology Series. pp 31–46
- Taddeucci J, Pompilio M, Scarlato P (2004) Conduit processes during the July–August 2001 explosive activity of Mt. Etna

- (Italy): inferences from glass chemistry and crystal size distribution of ash particles. *J Volcanol Geophys Res* 137:33–54
- Tatsumi Y (1986) Formation of the volcanic front in subduction zones. *Geophys Res Lett* 13(8):717–720
- Tatsumi Y, Eggins S (1995) *Subduction Zone Magmatism*. Blackwell Science, Cambridge, p 211
- Thompson AB (1992) Water in the Earth's upper mantle. *Nature* 358(6384):295–302
- Tormey DR, Frey FA, López-Escobar L (1995) Geochemistry of the Active Azufre—Planchon—Petroa volcanic complex, Chile (35°15'S): evidence for multiple sources and process in a Cordilleran Arc Magmatic System. *J Petrol* 36(2):265–298
- Venezky DY, Rutherford MJ (1999) Petrology and Fe-Ti oxide reequilibration of the 1991 Mount Unzen mixed magma. *J Volcanol Geoth Res* 89(1–4):213–230
- Wilson M (1989) *Igneous petrogenesis*. Kluwer, Boston